Mais informações no site da editora / Further information on publisher's website:

http://scripts.iucr.org/cgi-bin/paper?S2053229619011951

DOI: 10.1107/S2053229619011951

Acta Cryst C
STRUCTURAL
CHEMISTRY

ISSN 2053-2296

Analysis of solvent-accessible voids and proton-coupled electron transfer of 2,6-bis(1*H*-imidazol-2-yl)pyridine and its hydrochloride

Renan B. Guerra, Luis S. C. Huamaní, Juan C. Tenorio, Willian M. Guimarães, Juliano A. Bonacin and André Luiz Barboza Formiga*

Department of Inorganic Chemistry, University of Campinas – UNICAMP, 6154, Campinas, São Paulo 13083-970, Brazil. *Correspondence e-mail: formiga@unicamp.br

Received 24 June 2019
Accepted 29 August 2019

Edited by H. Uekusa, Tokyo Institute of Technology, Japan

Keywords: imidazole; crystal structure; proton-coupled electron transfer; DFT; electrochemistry; acid dissociation constant.

CCDC references: 1915852; 1915851

Supporting information: this article has supporting information at journals.iucr.org/c

The crystal structures of the solid form of solvated 2,6-bis(1*H*-imidazol-2-yl)-pyridine (H_2dimpy) trihydrate, $C_{11}H_9N_5{\cdot}3H_2O{\cdot}$[+solvent], **I**, and its hydrate hydrochloride salt 2-[6-(1*H*-imidazol-2-yl)pyridin-2-yl]-1*H*-imidazol-3-ium chloride trihydrate, $C_{11}H_{10}N_5^+{\cdot}Cl^-{\cdot}3H_2O$, **II**, are reported and analysed in detail, along with potentiometric and spectrophotometric titrations for evaluation of the acid–base equilibria and proton-coupled electron-transfer reactions. Compound **I** crystallizes in the high-symmetry trigonal space group $P3_221$ with an atypical formation of solvent-accessible voids, as a consequence of the 3_2 screw axis in the crystallographic *c*-axis direction, which are probably occupied by uncharacterized disordered solvent molecules. Additionally, the trihydrated chloride salt crystallizes in the conventional monoclinic space group $P2_1/c$ without the formation of solvent-accessible voids. The acid–base equilibria of H_2dimpy were studied by potentiometric and spectrophotometric titrations, and the results suggest the formation of H_3dimpy$^+$ (pK_{a1} = 5.40) and H_4dimpy^{2+} (pK_{a2} = 3.98), with the electrochemical behaviour of these species showing two consecutive irreversible proton-coupled electron-transfer reactions. Density functional theory (DFT) calculations corroborate the interpretation of the experimental results and support the assignment of the electrochemical behaviour.

1. Introduction

One of the most well-studied classes of ligands in an extensive range of applications is 2,2′:6′,2″-terpyridine (tpy) and its derivatives (Halcrow, 2005; Kershaw Cook *et al.*, 2013). 2,6-Bis(1*H*-imidazol-2-yl)pyridine (H_2dimpy; see Scheme 1) is a ligand with a very similar structure to that of tpy, bearing two imidazole rings attached to a central pyridine group, which makes it a rich N-containing heterocycle with an interesting σ-donor and π-accepting character.

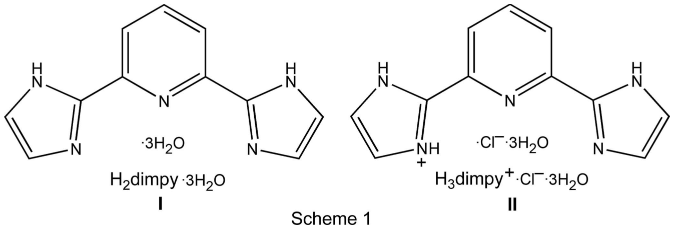

Scheme 1

The N—H group is highly versatile and can be easily modified through deprotonation or alkylation of the ligand for modulation of redox and electronic properties in coordination compounds, due to the change of electronic density in the metal centre, and it is also important in proton-coupled electron-transfer (PCET) reactions. These attributes make this

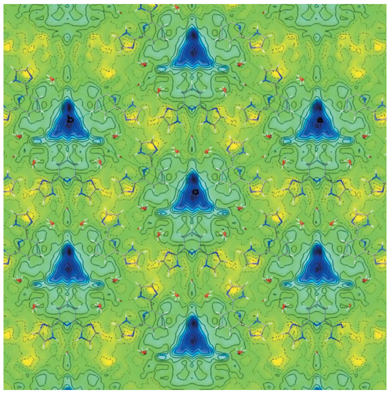

https://doi.org/10.1107/S2053229619011951

ligand very attractive for application in new compounds, including not only enhancement of photochemical and supramolecular features of the ligand itself, but also on the spectroscopic and redox chemistry of a wide range of 3*d* transition-metal complexes.

A literature survey on the chemistry of H_2dimpy showed the use of this molecule and its derivatives, *via* alkylation or deprotonation, in the modulation of redox and spectroscopic properties of Co, Mn, Ni, Ru and Fe complexes (Carina *et al.*, 1998; Fuchs *et al.*, 2010; Hammes *et al.*, 2005; Savchuk *et al.*, 2017; Stupka *et al.*, 2004), and in the preparation of catalysts based on different metal centres, for example, ruthenium(II) complexes for H/D exchange between hydrocarbons (Hashiguchi *et al.*, 2010) and for condensation of benzyl alcohol (Li *et al.*, 2018), copper(II) complexes for atom-transfer radical polymerization (Ratier de Arruda *et al.*, 2017) and cobalt(III) complexes for water oxidation (Rigsby *et al.*, 2012). Reports on gold(III) complexes as anticancer agents (Zou *et al.*, 2013) and organoplatinum(II) complexes with charge-carrier mobility and thermo- and vapour-luminescence properties (Che *et al.*, 2011) were also found in the literature.

However, despite the use and overall interest of this molecule in the synthesis of novel compounds, the crystalline structure has not yet been reported, unlike terpyridine and other widely used N-heterocyclic ligands. The data concerning the crystal structure of this molecule and the understanding of the intermolecular force interactions and hydrogen bonds in supramolecular crystal structures are crucial to trace the relationships between structure and properties, and valuable for the rational design of new compounds (Bibi *et al.*, 2018*a*; Taylor & Sausa, 2018; Bayar *et al.*, 2018; Latosińska *et al.*, 2014; Zeman *et al.*, 2010).

In this work, two previously unpublished structures are reported, namely $H_2dimpy{\cdot}3H_2O{\cdot}$[+solvent], where the structure includes an unknown disordered solvent (compound **I**), and $H_3dimpy^+{\cdot}Cl^-{\cdot}3H_2O$, a protonated hydrochloride acid derivative form (compound **II**). To complement the study and understanding of the system, the pK_a values were determined by potentiometric and spectrophotometric titration. Electrochemical and spectroscopic data combined with density functional theory (DFT) studies provided a substantial extent of knowledge regarding this molecule, which is of utmost importance for the future planning of new compounds.

2. Experimental

2.1. Material and apparatus

Sodium hydroxide (NaOH ≥98%), potassium chloride (KCl ≥99%) and potassium nitrate (KNO_3 ≥99%) were purchased from Sigma–Aldrich. Hydrochloric acid [$HCl_{(aq)}$ 37%] was purchased from Merck and methanol (MeOH, HPLC grade) was purchased from Tedia (Fairfield, OH, USA). All reactants were used as received without further purification. MilliQ water (Millipore Corporation, USA) was used in all experiments in aqueous media.

The pK_a determination was performed by pH potentiometric titration. The procedure consisted of the preparation of aqueous solutions (with 20% of methanol) of H_2dimpy 0.0075 mol l^{-1} (32 mg in 20 ml of MilliQ water, initial pH = 7.5) which were titrated against previously standardized solutions of HCl (0.089 mol l^{-1}) and NaOH (0.092 mol l^{-1}). Two titrations were performed with the addition of the acid and base *via* a micropipette (Eppendorf Research), and the pH change was registered after each addition of 10 µl. MilliQ water was boiled prior to the preparation of all solutions used. The pH variation was monitored using a pH meter Lab 827 from Metrohm with 0.01 resolution. The calibration was always carried out before measurements with buffer solutions (purchased from Labsynth) of pH 4.0, 7.0 and 10.0 at 25 ± 0.5 °C.

A similar procedure was used for the spectrophotometric pK_a determination in which 100 ml of H_2dimpy 3.5×10^{-5} mol l^{-1} in aqueous solution (5% methanol) was prepared as a stock solution. To make sure that the concentration of H_2dimpy would be constant through all the measurements, 25 ml of HCl 0.05 mol l^{-1} and NaOH 0.05 mol l^{-1} were prepared using the stock solution. Two titrations were performed with the addition of the acid and base solutions *via* a micropipette, recording a spectrum after each addition and pH change.

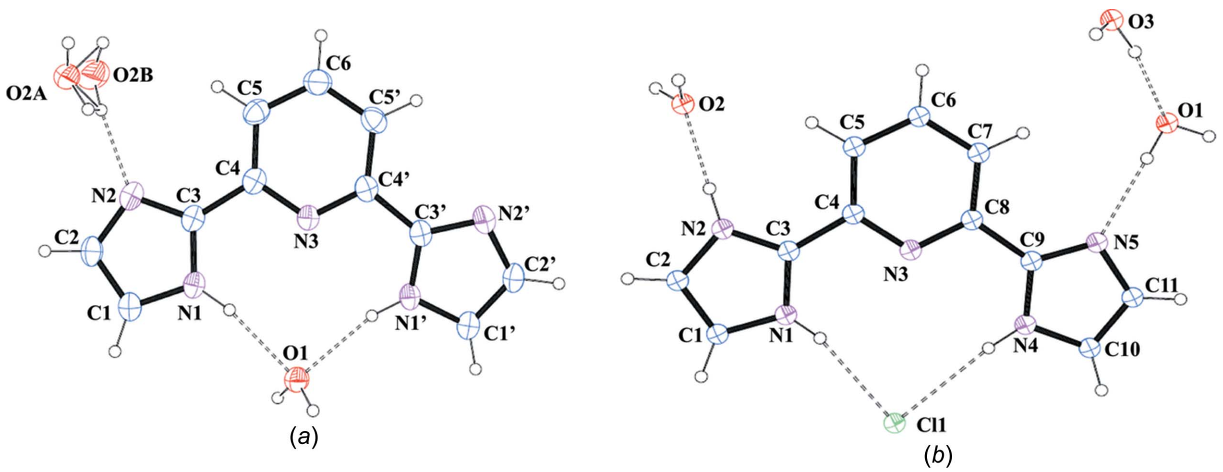

Figure 1
The molecular structures of (*a*) compound **I** and (*b*) compound **II**. Displacement ellipsoids are drawn at the 50% probability level.

Table 1
Experimental details.

Experiments were carried out at 150 K with Cu $K\alpha$ radiation using a Bruker APEX CCD-detector diffractometer. Absorption was corrected for by multi-scan methods (*SADABS*; Bruker, 2010).

	I	II
Crystal data		
Chemical formula	$C_{11}H_9N_5 \cdot 3H_2O \cdot$[+solvent]	$C_{11}H_{10}N_5^+ \cdot Cl^- \cdot 3H_2O$
M_r	265.28	301.74
Crystal system, space group	Trigonal, $P3_221$	Monoclinic, $P2_1/c$
a, b, c (Å)	18.6043 (5), 18.6043 (5), 3.9112 (1)	6.6577 (5), 22.6308 (16), 9.7566 (7)
α, β, γ (°)	90, 90, 120	90, 103.845 (3), 90
V (Å^3)	1172.38 (7)	1427.31 (18)
Z	3	4
μ (mm^{-1})	0.71	2.53
Crystal size (mm)	0.42 × 0.07 × 0.06	0.21 × 0.12 × 0.06
Data collection		
$T_{\min}$, $T_{\max}$	0.589, 0.753	0.541, 0.753
No. of measured, independent and observed [$I > 2\sigma(I)$] reflections	4574, 1416, 1375	12948, 2501, 2337
$R_{\rm int}$	0.035	0.037
$(\sin \theta/\lambda)_{\max}$ (Å^{-1})	0.603	0.595
Refinement		
$R[F^2 > 2\sigma(F^2)]$, $wR(F^2)$, S	0.038, 0.095, 1.12	0.030, 0.083, 1.08
No. of reflections	1416	2501
No. of parameters	107	208
No. of restraints	13	0
H-atom treatment	H-atom parameters constrained	H atoms treated by a mixture of independent and constrained refinement
$\Delta\rho_{\max}$, $\Delta\rho_{\min}$ (e Å^{-3})	0.19, −0.18	0.19, −0.26
Absolute structure	Flack x determined using 610 quotients $[(I^+) - (I^-)]/[(I^+) + (I^-)]$ (Parsons *et al.*, 2013)	–
Absolute structure parameter	−0.06 (13)	–

Computer programs: *APEX3* (Bruker, 2010), *SAINT* (Bruker, 2010), *SHELXT* (Sheldrick, 2015*a*), *SHELXL2018* (Sheldrick, 2015*b*), *OLEX2* (Dolomanov *et al.*, 2009), *ORTEP-3* (Farrugia, 2012) and *Mercury* (Macrae *et al.*, 2008).

Electrochemical measurements were performed on a Metrohm Autolab PGSTAT12 potentiostat (ECO Chemie, Utrecht, Netherlands), using a three-electrode cell consisting of a glassy carbon (3 mm diameter) working electrode, a standard calomel electrode (SCE) as a reference electrode and a Pt wire as an auxiliary electrode. For typical cyclic voltammetry experiments, a 0.1 mol l^{-1} KNO_3 aqueous solution (with 25% methanol) was used as an electrolyte with 1.0×10^{-3} mol l^{-1} H_2dimpy concentration. For evaluation of the dependence of oxidation potential ($E_{\rm ox}$) as a function of pH, an aqueous 0.1 mol l^{-1} Britton–Robinson (B–R) buffer solution was used as an electrolyte and the pH was changed with the addition of NaOH and HCl; the H_2dimpy concentration was 1.0×10^{-3} mol l^{-1}. The working electrode was prepolished with 0.1, 0.05 and 0.03 µm alumina paste and washed with water–ethanol (1:1 *v*/*v*).

For the spectroelectrochemical measurements, a Metrohm Autolab PGSTAT12 potentiostat was used with a diode array HP Agilent 8453 spectrophotometer that can work in the 190–1100 nm range and record two spectra per second. The working electrode, in this case, was a platinum grid electrode, with a standard calomel electrode (SCE) as a reference electrode and a Pt wire as an auxiliary electrode, with a 1 mm optical path length for the electrochemical cell. A 3.5×10^{-4} mol l^{-1} solution of H_2dimpy was prepared using 0.1 mol l^{-1} KCl as electrolyte instead of KNO_3 due to the strong UV absorption by KNO_3.

2.2. Synthesis and crystallization

2,6-Bis(1*H*-imidazol-2-yl)pyridine (H_2dimpy) was synthesized following procedures described in the literature (Voss *et al.*, 2008; Hashiguchi *et al.*, 2010; Rigsby *et al.*, 2012), with minor modifications (see the supporting information for a detailed description). Single crystals suitable for diffraction analysis were obtained by slow recrystallization from a methanol–water (3:1 *v*/*v*) solution for compound **I** and a methanol–HCl (0.1 mol l^{-1}) (9:1 *v*/*v*) solution for compound **II**, by dissolving 10 mg of H_2dimpy in 5 ml of the corresponding mixture and placing it in a 10 ml vial with a needle-perforated lid at room temperature for 5 d, after which time the crystals were collected.

2.3. Data collection and refinement

Crystal data, data collection and structure refinement details are summarized in Table 1. H atoms were treated by a mixture of independent and constrained refinement. In compound **I**, the C, N and O-bound H atoms were positioned geometrically and refined using a riding model, with aromatic C—H = 0.95 Å, N—H = 0.88 Å and water O—H = 0.87 Å, and with $U_{\rm iso}$(H) = $1.2U_{\rm eq}$(C,N) for aromatic H atoms and $1.5U_{\rm eq}$(O) for water H atoms. Due to the better quality diffraction data obtained for compound **II**, it was possible to locate the H atoms in a difference Fourier map and refine their positions freely, but using $U_{\rm iso}$(H) = $1.2U_{\rm eq}$(C,N) and $1.5U_{\rm eq}$(O) conditions for the H-atom displacement parameters. The positional disorder of the water molecules in **I** was modelled over positions O2*A* and O2*B* using free variables to refine the site-occupancy factors, which yielded an occupancy ratio of 0.290 (16):0.710 (16). The *OLEX2* solvent-mask routine (Dolomanov *et al.*, 2009) was employed to mask out the residual electron density of the disordered solvent molecules using a probe radius of 1.2 Å, which calculated a volume fraction of 218.1 Å^{-3} and 70 electrons per unit cell in the solvent-accessible voids, which is discussed in further detail in §3.1.

2.4. Computational methods

Density functional theory (DFT) calculations were performed with the B3LYP functional (Becke, 1993; Lee *et al.*, 1988) and the def2-TZVP basis set (Weigend & Ahlrichs, 2005) for all atoms using *ORCA* software (Release 4.0.1; Neese, 2012). The effect of water as an implicit solvent was assessed using the C-PCM (Barone & Cossi, 1998) method with the standard implementation in the software. This choice of functional, basis set and implicit solvation is well known to give reliable results for protonation and tautomeric equilibria in solution and it has been used over the years by our group (Abbehausen *et al.*, 2012; Bibi *et al.*, 2018*b*; Timm *et al.*, 2008; Bonacin *et al.*, 2007). In all calculations, the RIJCOSX approximation (Izsák & Neese, 2011) and auxiliary functions (Weigend, 2006) were employed with convergence criteria of 1.0×10^{-8} Eh for the energies and 1.0×10^{-4} Eh/a$_0$ for the gradients in geometry optimizations. All geometries were confirmed as minima through the calculation of the Hessians.

DFT results were used to obtain theoretical p$K_{\rm a}$ and oxidation potentials using thermodynamic cycles as previously established (Keith *et al.*, 2013). In brief, p$K_{\rm a}$ values were calculated with an isodesmic strategy using formate/formic acid as the standard experimental p$K_{\rm a}$ value in comparison

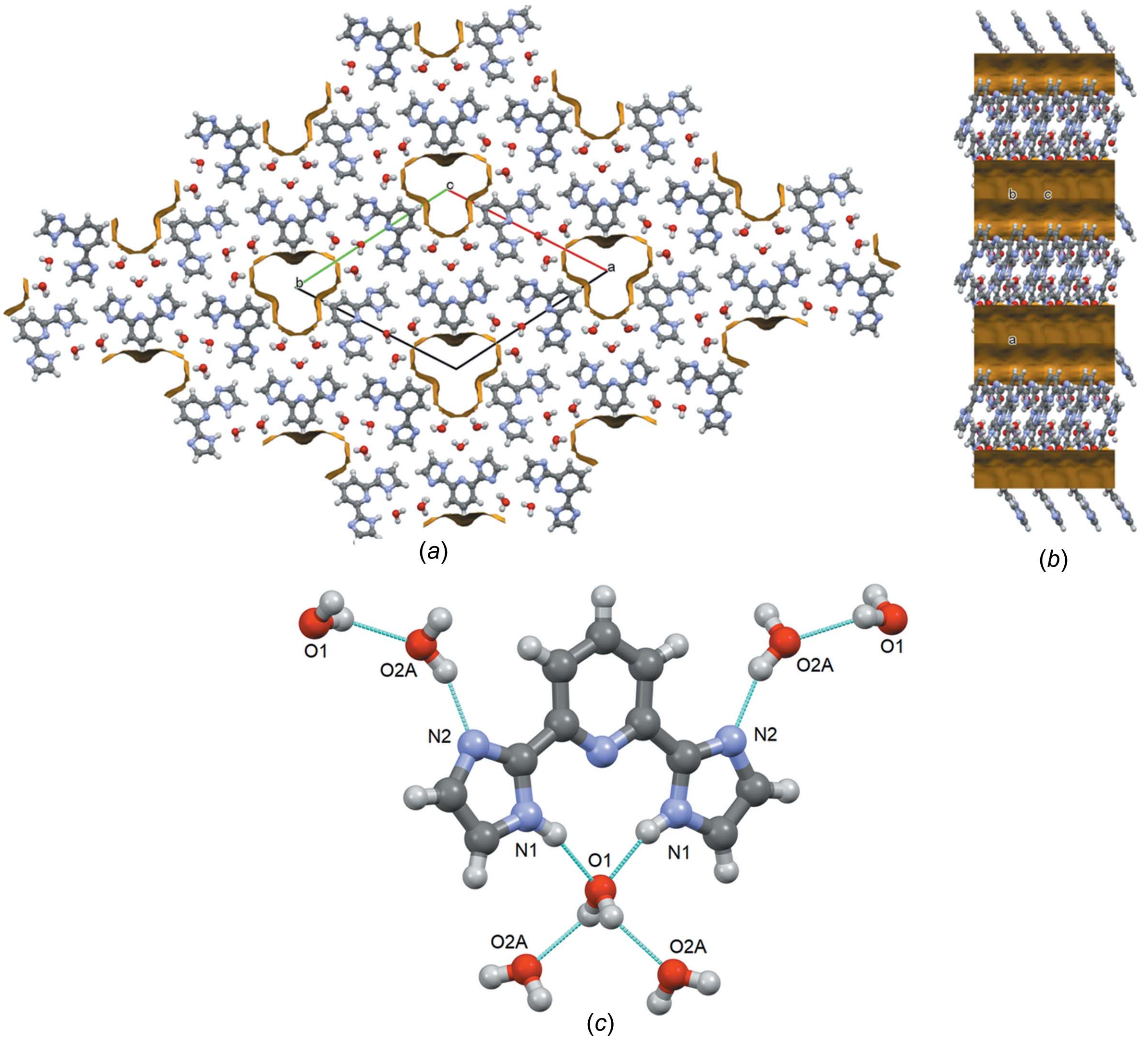

(*a*)
(*b*)
(*c*)

Figure 2
Crystal packing views of compound **I** in the (*a*) [001] and (*b*) [100] directions. Solvent-accessible voids are depicted with yellow surfaces. (*c*) The main hydrogen bonds around the molecule of **I**. The disordered O2*B* water molecule has been omitted for clarity.

with a series of N-heterocycles with known pK_a values. From these calculations, a calibration curve was obtained, from which the theoretical pK_a values for all protonation states of H_2dimpy were calculated. Using another thermodynamic cycle, the oxidation potentials for H_2dimpy in all protonation states were calculated, using -4.281 V as the energy of the free electron referenced to the absolute standard hydrogen electrode (SHE) in water (Isse & Gennaro, 2010). These DFT predicted potentials were further shifted by 0.241 V to be in the same scale as the experimental results (*versus* a saturated calomel electrode, SCE). The supporting information includes detailed information for both types of calculations.

3. Results and discussion

3.1. Crystal structures

Compound **I** crystallizes in the high-symmetry trigonal space group $P3_221$ (see further crystal structure details in Table 1). The asymmetric unit (Fig. 1*a*) is localized in a special position in which a twofold axis passes through the H_2dimpy molecule (intercepting the N1 and C3 atoms of the central pyrimidine ring) and one of the water molecules also. Moreover, a disordered water molecule occupying two positions is also observed. The crystal packing exhibits an interesting behaviour, due to the crystalline symmetry of this space group, in which solvent-accessible voids are formed as a consequence of the presence of the 3_2 screw axis in the crystallographic *c*-axis direction (see Figs. 2*a* and 2*b*), resulting in the formation of channels that run along this direction.

Meaningful peaks of residual electron densities were observed in these solvent-accessible voids, which in principle are associated with solvent molecules. However, it was not possible to identify the solvent, nor obtain a satisfactory disorder model for the solvent molecules around the structural void, mainly due to the residual peaks being located near special positions, specifically over the twofold symmetry axes intercepting the threefold axis, which leads to an unrefinable modelling of molecules in these regions. Therefore, it was proposed to use the *OLEX2* solvent Mask routine (Dolomanov *et al.*, 2009), analogous to the *PLATON*/SQUEEZE routine (Spek, 2009, 2015), in order to mask out the extremely disordered density around the solvent-accessible voids (see Fig. 3). The initial structural refinement, without considering any kind of solvent molecule, gave the refinement indexes $R1$ = 0.0748 [$F_o > 4\sigma(F_o)$] and $wR2$ = 0.1970. Trying to model two methanol molecules in which one of them has a site occupation factor (sof) of 0.36, the refinement indexes dropped to $R1$ = 0.0420 [$F_o > 4\sigma(F_o)$] and $wR2$ = 0.1086. Whereas, modelling one methanol molecule lying over a twofold axis and with partial occupancy (sof = 0.80) and one water molecule close to the threefold axis, the refinement indexes are $R1$ = 0.0468 [$F_o > 4\sigma(F_o)$] and $wR2$ = 0.1232. Lastly, after the utilization of the *OLEX2* solvent mask, the refinement indexes dropped to $R1$ = 0.0366 [$F_o > 4\sigma(F_o)$] for 4576 unique reflections and $wR2$ = 0.0991. The volume fraction was calculated to be 218.1 Å^{-3} and 70 electrons per unit cell were allocated. From that it is possible to expect the presence of two methanol molecules, with one of them having a low occupancy factor, or one methanol molecule with partial occupancy and one water molecule pivoted around the threefold axis. These possibilities coincide with the quantity of electrons calculated by the solvent-mask routine, which has proved to be the best strategy to establish a coherent model for this structure.

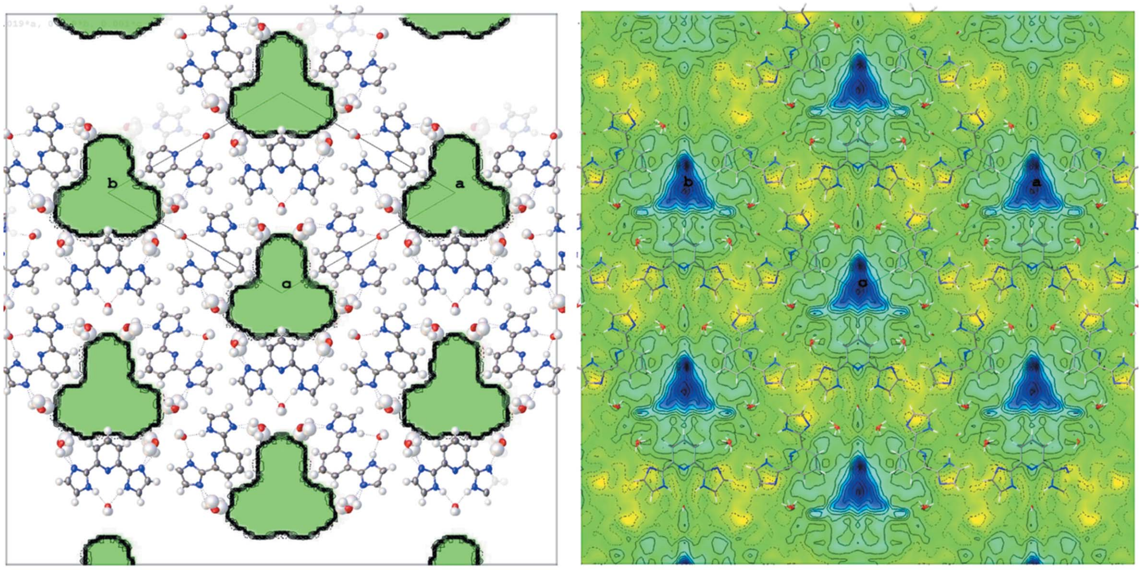

(*a*) (*b*)

Figure 3
(*a*) Mapping of the solvent-mask procedure over the solvent-accessible voids in compound **I**. (*b*) A residual electron-density contour map, depicting the extremely disordered electron density around the solvent-accessible voids. The maps corresponding to the crystal packing viewed in the [001] direction. The contours are drawn at 0.1 e Å^{-3}. The blue contours depict positive residual electron density.

Although the disorder models for the bulk solvent molecules were not satisfactory, they do not seem to play an important role in the structural conformation of the H_2dimpy molecules.

It has been observed before that this behaviour is particularly common in some crystal structures that crystallize in trigonal and hexagonal space groups (Braun *et al.*, 2015). A well-known case is the mono-component polymorph of the carbamazepine drug molecule [called form II or α-carbamazepine; Cambridge Structural Database (CSD; Groom *et al.*, 2016) refcode CBMZPN03 (Lowes *et al.*, 1987)], which crystallizes in the space group $R\overline{3}$ and shows solvent-accessible voids of 9% of the unit-cell volume. This phenomenon in carbamazepine has been studied by several researchers to comprehend the meaning of the solvent-accessible voids, their thermodynamic properties, as well as the possibility to solvent inclusion in the structure, in order to predict even pharmaceutical properties (Lowes *et al.*, 1987; Fabbiani *et al.*, 2007; Cruz Cabeza *et al.*, 2007). A rigorous study by Braun *et al.* (2015) regarding the polymorphic solid forms of 4-aminoquinaldine, reported the presence of solvent-accessible voids in $R\overline{3}$ structures, obtained by experimental and theoretical methods. All the studies reveal the tendency of these trigonal structures to form solvent-accessible voids larger than 6.0% of the unit-cell volume when compared to crystal energy landscape values, mainly over the regions of the roto-inversion axis giving rise to the formation of channels as isolated sites, in which guest molecules (*e.g.* solvents) can be located. In a recent search in the CSD we were able to recover a total of 268 hits for organic molecule structures that crystallize in the trigonal space group $P3_221$, of which only 10.0% show solvent-accessible voids greater than 8.0% of the unit-cell volume. Despite the low occurrence of these kinds of voids in $P3_221$ when compared to $R\overline{3}$, it is clear that, in some cases, there is a tendency for solvent-accessible voids to form in trigonal space groups as a consequence of the threefold axis in the presence of symmetric molecules, as happens in H_2dimpy. The inclusion of solvent molecules in the voids is also observed in α-carbamazepine and 4-aminoquinaldine polymorphs (Lowes *et al.*, 1987; Fabbiani *et al.*, 2007). In both cases, the solvent-accessible voids occur at special positions. This feature appears to be usual for these kinds of structures.

Table 2
Hydrogen-bond geometry (Å, °) for **I**.

D—H$\cdots A$	D—H	H$\cdots A$	$D\cdots A$	D—H$\cdots A$
N1—H1$A\cdots$O1	0.88	2.05	2.900 (2)	163
O1—H1$B\cdots$O2B^{i}	0.87	2.07	2.823 (5)	144
O1—H1$B\cdots$O2A^{i}	0.87	2.19	2.719 (7)	119
O2B—H2$BB\cdots$N2	0.87	1.93	2.734 (4)	153
O2A—H2$AB\cdots$N2	0.87	2.03	2.740 (7)	138

Symmetry code: (i) $-y+1, x-y, z+\frac{2}{3}$.

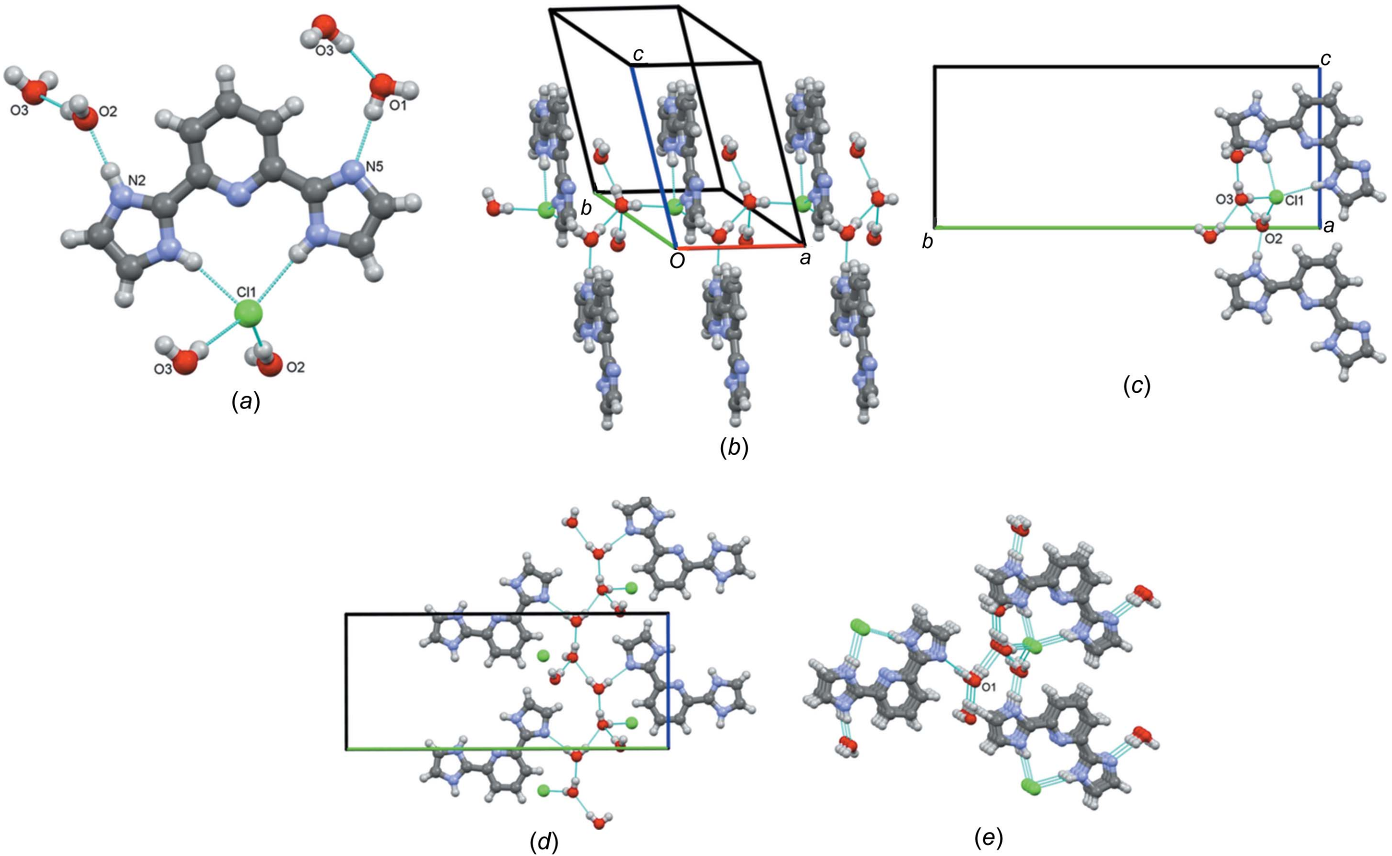

Figure 4
(a) The hydrogen bonds observed in **II**. (b)/(c) Views of the O2$\cdots$Cl1$^-\cdots$O3 chain in the [010] and [100] directions, respectively. (d) The water molecule ribbons. (e) The role of the O1 water molecules in the crystal packing.

Regarding the molecular structure, H_2dimpy shows an approximately coplanar conformation between the pyridine (Pyr) and imidazole (Imi) rings (Fig. 1*a*). As commented on above, half of the H_2dimpy molecule is reproduced by twofold rotation axis symmetry. Taking that into account, we determined the least-squares mean plane through half of the atoms of the pyridine ring and one of the imidazole rings, and determined a dihedral angle between the two least-squares mean planes of 6.272 (6)°, which demonstrates a slight distortion from planarity. The C3—C4 bond has a length of 1.465 (3) Å and is responsible for the linkage between the Pyr and Imi rings. This bond length is typical of σ-bonds between Csp^2 atoms. From the Fourier maps, it was possible to determine that the N—H group of the Imi ring is *syn*-orientated with respect to the N3 atom of the Pyr ring. The φ(N1—C3—C4—N3) torsion angle of 5.6 (2)° agrees with this conformation and further structural parameters are listed in the supporting information.

Table 3
Hydrogen-bond geometry (Å, °) for **II**.

D—H···*A*	*D*—H	H···*A*	*D*···*A*	*D*—H···*A*
N1—H1···Cl1	0.82 (2)	2.35 (2)	3.1508 (13)	166 (2)
N2—H2···O2^{i}	0.86 (2)	1.82 (2)	2.6762 (17)	178 (2)
N4—H4···Cl1	0.86 (2)	2.43 (2)	3.2907 (13)	174 (2)
O1—H1*B*···O3^{ii}	0.87 (2)	2.03 (2)	2.8839 (16)	169 (2)
O1—H1*C*···N5^{iii}	0.84 (2)	2.00 (2)	2.8359 (18)	178 (2)
O2—H2*B*···Cl1	0.88 (2)	2.21 (2)	3.0900 (13)	177 (2)
O2—H2*C*···O3	0.82 (2)	1.90 (2)	2.7230 (17)	177 (2)
O3—H3*A*···Cl1^{iv}	0.80 (2)	2.33 (2)	3.1223 (12)	171 (2)
O3—H3*B*···O1	0.86 (2)	1.89 (2)	2.7359 (17)	169 (2)

Symmetry codes: (i) $x, y, z+1$; (ii) $x, -y+\frac{1}{2}, z+\frac{1}{2}$; (iii) $-x+1, -y, -z+1$; (iv) $x+1, y, z$.

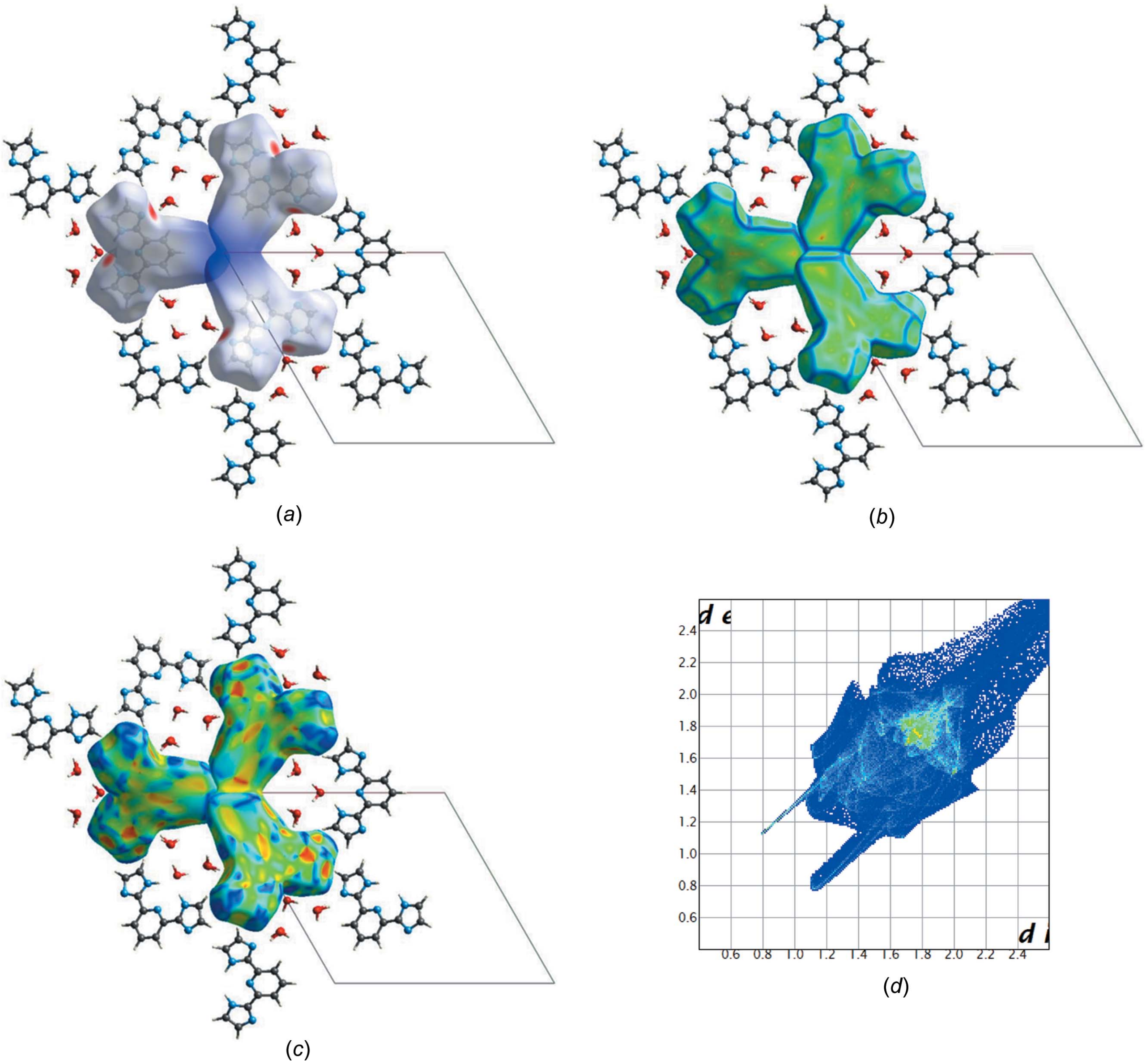

(*a*) (*b*) (*c*) (*d*)

Figure 5
The Hirshfeld surface of compound **I**, with (*a*) $d_{\rm norm}$, (*b*) curvedness and (*c*) shape-index surfaces, and (*d*) the 2D fingerprint plot.

The crystal structure indicates strong hydrogen bonds (HBs) between the H_2dimpy and water molecules, which form the crystal packing around the symmetry of the 3_2 screw axis. Initially, a bifurcated N1—H1···O1 HB was observed between the N—H fragments of the Imi rings and one of the water molecules (O1), which lies over the twofold axis (see Table 2 and Fig. 2*c* for the hydrogen-bond parameters). Simultaneously, this water molecule acts as a donor of two O1—H···O2*A* HBs with two water molecules (O2) due to the twofold axis symmetry. Conversely, the O2 water molecules, which are partially disordered due to their proximity to the solvent-accessible voids, work like a bridge between the O1 water molecule and the other reticular H_2dimpy molecules through the HB O2*A*—H···N2 interactions, which are facilitated by the presence of a single pair of electrons on the N2 atoms in the Imi rings. Despite Braun *et al.* (2015) having suggested that large solvent-accessible voids are not energetically favoured in comparison to the more closely packing voids, in H_2dimpy, the occurrence of HBs with the included water molecules in the crystal lattice allows the stabilization of the crystal structure (Braun *et al.*, 2015). On the other hand, π–π interactions are observed between Pyr···Pyr and Imi···Imi rings, stacked along the crystallographic *c* axis, resulting in parallel helical columns around the 3_2 screw axis with a centroid–centroid (*Cg*···*Cg*; symmetry code: *x*, *y*, $-z + 1$) distance of 3.9112 (10) Å and an offset angle between the centroids of 29.9°. The extremely disordered molecules allocated to the regions of the solvent-accessible voids do not furnish any kind of meaningful intermolecular interactions.

Compound **II** is a hydrochloride salt that crystallizes in the conventional monoclinic space group $P2_1/c$, with one ion pair and three water molecules occupying a non-equivalent position in the asymmetric unit (Fig. 1*b*). From the difference Fourier maps, the residual electron densities associated with the H-atom positions were visualized, and hence it was possible to determine that the protonation of H_2dimpy preferably takes place in one of the five-membered rings, namely the Imi-*A* ring (composed of atoms N1/C1/C2/N2/C3). A ring relaxation in Imi-*A* is observed, with C1—N1—C3 and C2—N2—C3 bond angles of 109.25 (5) and 108.88 (5)°, respectively, which are larger than those observed in the Imi-*B* ring, whose C9—N4—C10 and C9—N5—C11 angles are 107.48 (6) and 104.93 (5)°, respectively, confirming that protonation occurs predominantly in the Imi-*A* ring. Moreover, the angles of the Imi-*A* ring are also larger than the corresponding angles observed in **I** [C1—N1—C3 = 108.04 (18)° and C2—N2—C3 = 104.86 (18)°]. The molecular conformation of **II** presents a more planar conformation than **I**, wherein the dihedral angles of the least-squares mean planes of the Pyr and the Imi-*A* and Imi-*B* rings are 2.455 (1) and 0.796 (2)°, respectively. Therefore, protonation in one of the Imi rings leads to an increase in the planarity of the structure

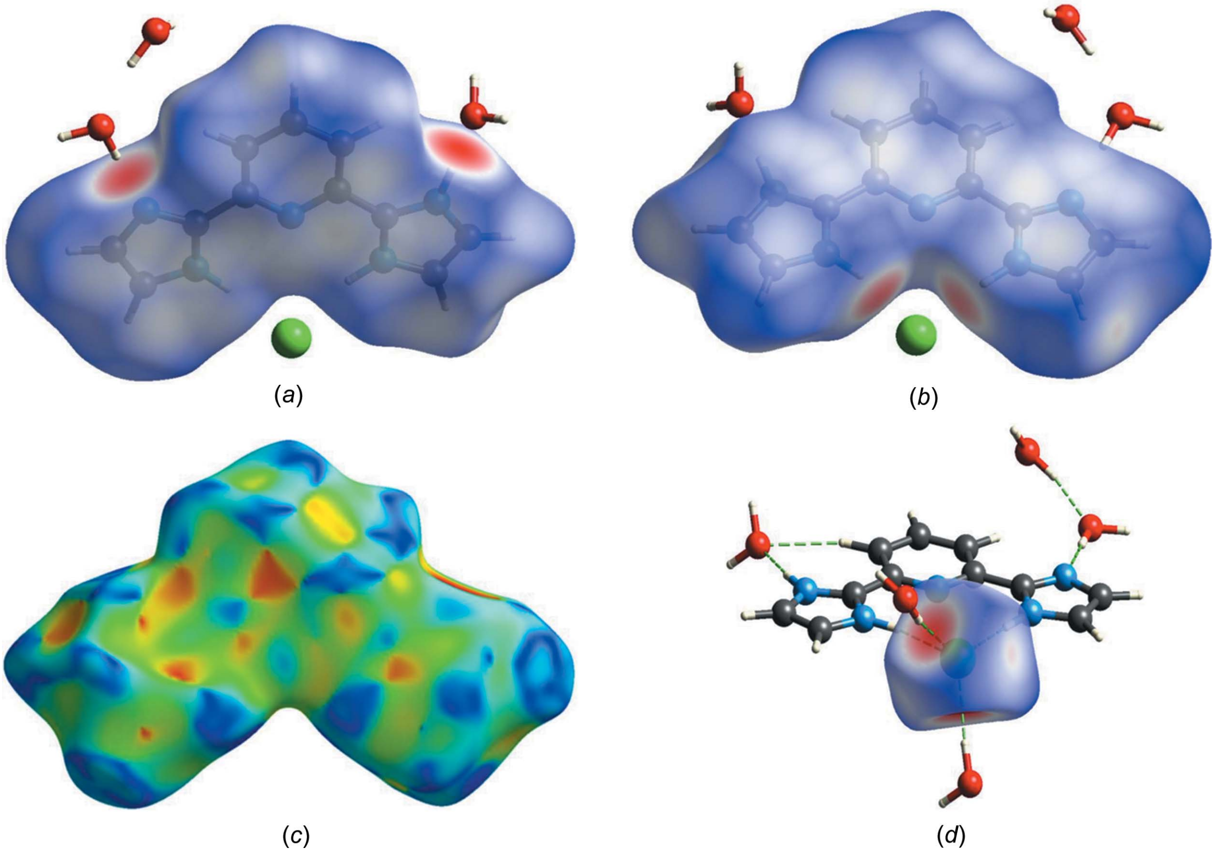

Figure 6
View of the $d_{\rm norm}$ surface of (*a*) the front and (*b*) the back face in the H_3dimpy$^+$ unit on **II**. (*c*) Shape-index surface and (*d*) enclosed $d_{\rm norm}$ surfaces of the Cl^- anion.

when compared to **I**. Similar to H$_2$dimpy, the N—H fragments of the Imi rings are *syn*-oriented with respect to the pyridine N3 atom, in which the torsion angles φ(N3—C4—C3—N1) and φ(N3—C8—C9—N4), with values of 2.26 (18) and −0.23 (18)°, respectively, are characteristic of this conformation. The crystal packing is likely stabilized by HB interactions. Initially, the ionic pair is stabilized by bifurcated N—H$\cdots$Cl$^-$ interactions, through N1—H1$\cdots$Cl$^-$ and N4—H4$\cdots$Cl$^-$ HBs (see Table 3), forming a graph-set $R_2^1(10)$ motif (Etter, 1990).

The HB pattern shown in Fig. 4(*a*) resembles that observed in **I** in that the Cl$^-$ anion in **II** occupies a similar position to one water molecule in **I**. The Cl$^-$ anions adopt an almost planar conformation with respect to the least-squares mean plane of the Pyr ring, positioned at a distance of 0.0193 (10) Å from this plane. These anions interact with two water molecules through strong HBs of the O2—H$\cdots$Cl1$^-$ and O3—H$\cdots$Cl1$^-$ types, resulting in the formation of chains (see Figs. 4*b* and 4*c*) which grow along the crystallographic [001] direction. The O1 water molecules reinforce the crystal packing, acting like bridges through strong O2—H$\cdots$O1 HBs between the hydrophilic O2$\cdots$Cl1$^-\cdots$O3 chains in [100] and the cationic molecules (H$_3$dimpy$^+$) through the O1—H$\cdots$N5 interactions depicted in Figs. 4(*d*) and 4(*e*). At the same time, H$_3$dimpy$^+$ cations interact directly with the O2$\cdots$Cl1$^-\cdots$O3 chains through the N2—H$\cdots$O2 HB, giving a close packing along the [100] direction. On the other hand, strong O3—H$\cdots$O1 and O1—H$\cdots$O3 HBs increase the stability of the crystal packing, forming ribbons of water molecules along the [001] direction. Moreover, an offset π-staking is also observed in the [100] direction between the H$_3$dimpy$^+$ cations, which are arranged in a distribution of interplanar layers separated by 3.320 Å.

3.2. Hirshfeld surface analysis

The analysis of the Hirshfeld surface (HS), which is based on the method of electron-density partitioning by a weight function (w) (Spackman & Jayatilaka, 2009), allows one to gain a detailed insight into the crystal packing (McKinnon *et al.*, 2004). In addition, the 2D fingerprint plots derived from the corresponding HS help in the comprehension of the supramolecular behaviour and the characterization of each solid form, since a 2D fingerprint plot is unique for each crystal structure (Spackman & McKinnon, 2002). These plots are represented by the external (d_e) and internal (d_i) distances of an atom to the surface. As a result, we see a scatterplot in which each coloured spot represents a possible contact defined by the sum of the distances (which should be in the same order as the sum of the van der Waals radii), as well as the contribution or intensity of this contact over the surface (McKinnon *et al.*, 2004; Spackman & McKinnon, 2002). This analysis was carried out using *CystalExplorer* (CE; Turner *et al.*, 2017).

The HS of the H$_2$dimpy in **I** (without considering the water molecules) shows an anomalous behaviour, which was expected due to the presence of the solvent-accessible voids in the crystal packing. This behaviour has been observed as well by Fabbiani *et al.* (2007) in the carbamazepine form II polymorph, in which the HS of H$_2$dimpy looks quite elongated beyond the pyridine ring, at the same time pivoting around the 3_2 screw axis localized at the centre of the structural void. The normalized distances (d_norm) surface (see Fig. 5*a*) clearly shows the regions of the HB contacts (red spots) over the N atoms of the imidazole rings. Both the shape-index and curvedness surfaces (Figs. 5*b* and 6*c*) reveal the regions where the π-interactions are happening, mainly in the regions nearest to the Pyr and Imi centroids, as discussed above. The 2D fingerprint plot (Fig. 5*d*) is quite spread out for the set of highest distances (d_e,d_i), featuring the disorder and the presence of the structural void in the structure (Braun *et al.*, 2015; Fabbiani *et al.*, 2007). The sharp peak centred at the left side of the graph diagonal (at a distance of $d_\mathrm{e} + d_\mathrm{i}$ = 1.9 Å) belongs to N—H$\cdots$O HB contacts between the N—H fragments of Imi rings and the water molecule that lies on the twofold axis. The broad spike on the right side of the diagonal graph is related to the HB contacts between the imidazole N

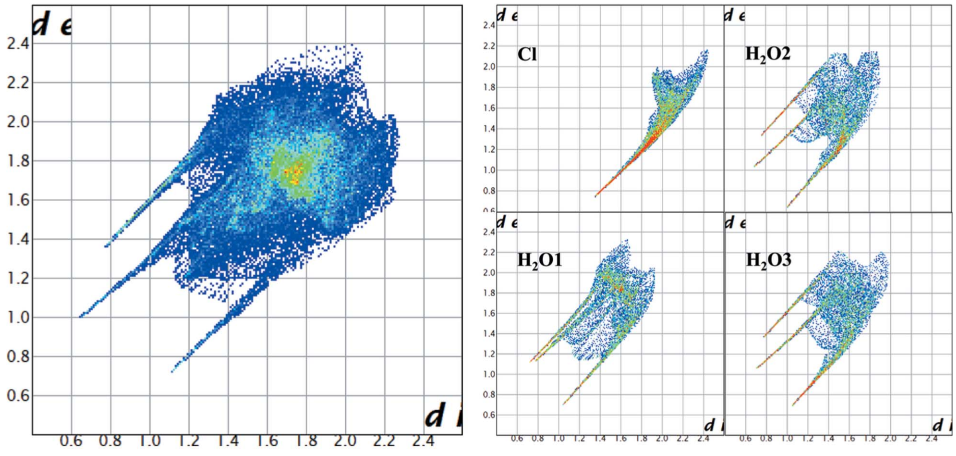

(*a*) (*b*)

Figure 7
2D fingerprint plots of the enclosed HS of (*a*) H$_3$dimpy$^+$ units and (*b*) each of components in compound **II**.

atoms and the disordered water molecules. The intense yellow spot centred at $d_e = d_i = 1.80$ Å corresponds to the C···C and C···N contacts involved in the onset π-stacking.

The HS that encloses the H_3dimpy^+ cations in **II** is a little asymmetric and deformed in the region of one of the Imi rings as a consequence of the protonation (Figs. 6*a* and 6*b*). From the d_{norm} surfaces can be clearly observed the red spot regions associated with the contacts involved in the HB of the H_3dimpy^+ cations with the Cl^- anions and the O1 and O2 water molecules. On the other hand, the d_{norm} HS enclosing the Cl^- anion shows intense contacts of the $H\cdots Cl^-$ type between the Cl^- anion and the water molecules, which contribute to the stabilization of the crystal structure (Fig. 6*d*). The shape-index surface of H_3dimpy^+ also gives evidence of the π-stacking due to adjacent red and blue triangles close to the centroids of the Pyr and Imi rings (Fig. 6*c*).

The 2D fingerprint plot observed for the HS enclosing only the H_3dimpy^+ cation, shows a spread out distribution, mainly associated with the H···H and C···H contacts, which together represent 61.1% of the contacts over the surface (see Fig. 7*a*). The sharp spike centred at $d_e = 0.7$ Å and $d_i = 1.1$ Å corresponds to the N···H contact, with a contribution of 6.3%, which is involved in O1—H···N5 interactions. Likewise, the sharp spike centred at $d_e = 1.0$ Å and $d_i = 0.65$ Å, with a contribution of 6.0%, corresponds to the O···H contact associated with the N2—H···O2 interaction between the protonated Imi ring and one of the water molecules. Both interactions contribute to the surface with similar percentages despite the N—H···O interaction being shorter. The most external spike on the left side of the plot diagonal, centred at $d_e = 1.4$ Å and $d_i = 0.8$ Å, is associated with the Cl···H contacts involved in $N—H\cdots Cl^-$ interactions, with a contribution of 7.2%, which help in the stabilization of the ionic pair. As observed in **I**, the intense yellow spot centred at $d_e = d_i = 1.8$ Å, corresponding mainly to the C···C contacts, with a contribution of 4.7%, confirms the presence of π-interactions also in this crystal structure. The 2D fingerprint plots from the HS enclosing the Cl^- anion and each of the water molecules are depicted in Fig. 7(*b*).

3.3. pK_a determination and electrochemical properties

The presence of two Imi groups suggests that a bis-protonated species may exist, but we were not able to isolate a crystal containing it, either using stoichiometric mixtures of the sample and hydrochloric acid or with acid in excess, with and without the addition of methanol. In order to understand possible reasons for the lack of success, we have performed solution studies aimed at the determination of the species in equilibrium under several conditions of pH.

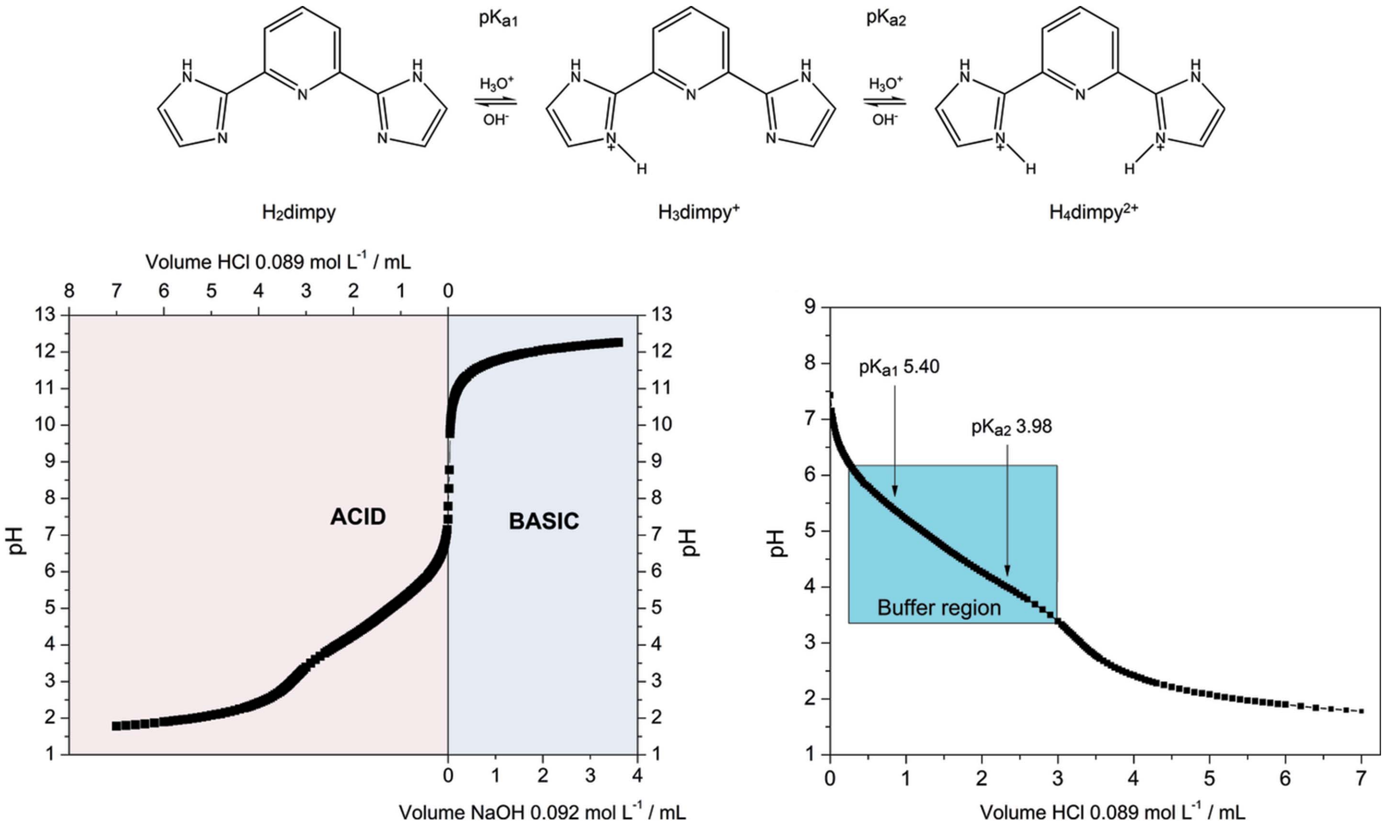

(*a*) (*b*)

Figure 8

(*a*) pH potentiometric titration curves of H_2dimpy (1.5×10^{-4} mol l^{-1}) in aqueous solution (20% methanol). The image shows the results from two titrations, one with the addition of HCl 0.089 mol l^{-1} (left side, red) and the other with the addition of NaOH 0.092 mol l^{-1} (right side, blue). (*b*) pH potentiometric titration of H_2dimpy (1.5×10^{-4} mol l^{-1}) with HCl 0.089 mol l^{-1}.

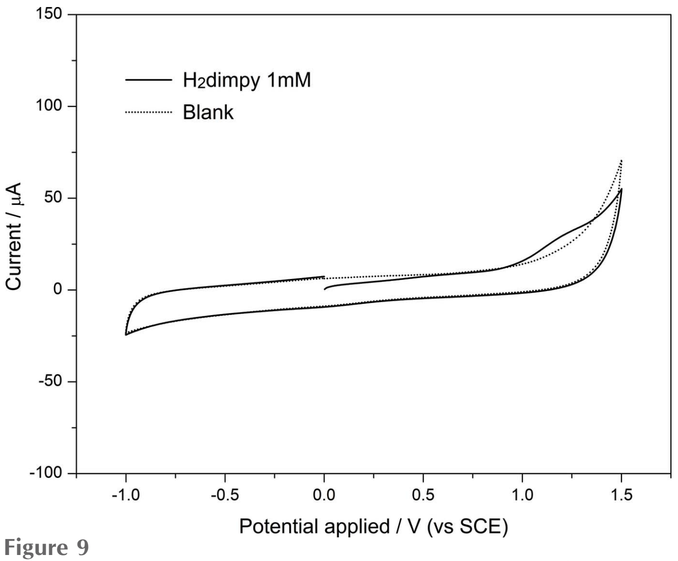

Figure 9
Cyclic voltammogram (CV) of H_2dimpy [1.0×10^{-3} mol l^{-1}] in water–methanol (4:1 *v*/*v*) (pH 5.57, 0.1 mol l^{-1} KNO_3) at 100 mV s^{-1}.

The potentiometric titration was performed following routine methods and addition of methanol was necessary to avoid precipitation under alkaline conditions. Using the results from the titration curve (Fig. 8*a*), only one change can be noticed on the acid part, suggesting a single protonation event. However, a close analysis in the acid titration (Fig. 8*b*) reveals a buffer region in the 3–6 pH range, an unusual value since a standard buffer region usually spreads by only 1 pH unit around the pK_a values. Moreover, the stoichiometry of the reaction confirms two equivalents of HCl at the final point, reinforcing that protonation of both imidazole groups was taking place. This led us to suggest that two protonations were taking place with very close pK_a values, thus making impossible the determination of their values by means of the first and second derivatives method (Adamczyk-Woźniak *et al.*, 2019).

In order to determine the experimental values, we simulated the profile of the potentiometric titration curve using *CurtiPlot 4.3.0* software (Gutz, 2018), resulting in a very good fitting of the experimental data with two protonation equilibria, as shown in Fig. S13 (see supporting information). The pK_a values found were 5.40 for the first protonation (pK_{a1}) and 3.98 for the second protonation (pK_{a2}). No changes at lower pH (between pH 1–3) were observed and no indication of deprotonation of H_2dimpy was observed in basic media. The pK_a value of the pyridine group is probably negative and thus not observed in our experiments, similar to the deprotonation of H_2dimpy and the formation of Hdimpy$^-$ that is expected to occur at a pH of above 14.

The pK_a values of the analogue molecule 2-(1*H*-imidazol-2-yl)pyridine (Himpy) have been reported by Eilbeck & Holmes (1967). For Himpy, the authors found a pK_a value of 5.47 for the protonation of the imidazole group, also determined by potentiometric titration, which is in very close agreement with the first pK_a value found in this study. These authors also estimated the pK_{a2} at approximately −0.7 by UV–Vis spectroscopy, which corresponds to the second protonation of the molecule in the pyridine portion.

The potentiometric titration results were also confirmed by UV–Vis spectrophotometric titration (Fig. S14 in the supporting information) and DFT simulation (Fig. S18 in the supporting information). The calculated pK_a values are 4.7 and 3.3 for pK_{a1} and pK_{a2}, respectively, in very good agreement with the experimental values. Theoretical results also show that the protonation of the pyridine ring would happen with a theoretical pK_a value of −10.9 and deprotonation of one imidazole ring (yielding Hdimpy$^-$) would have a pK_a of

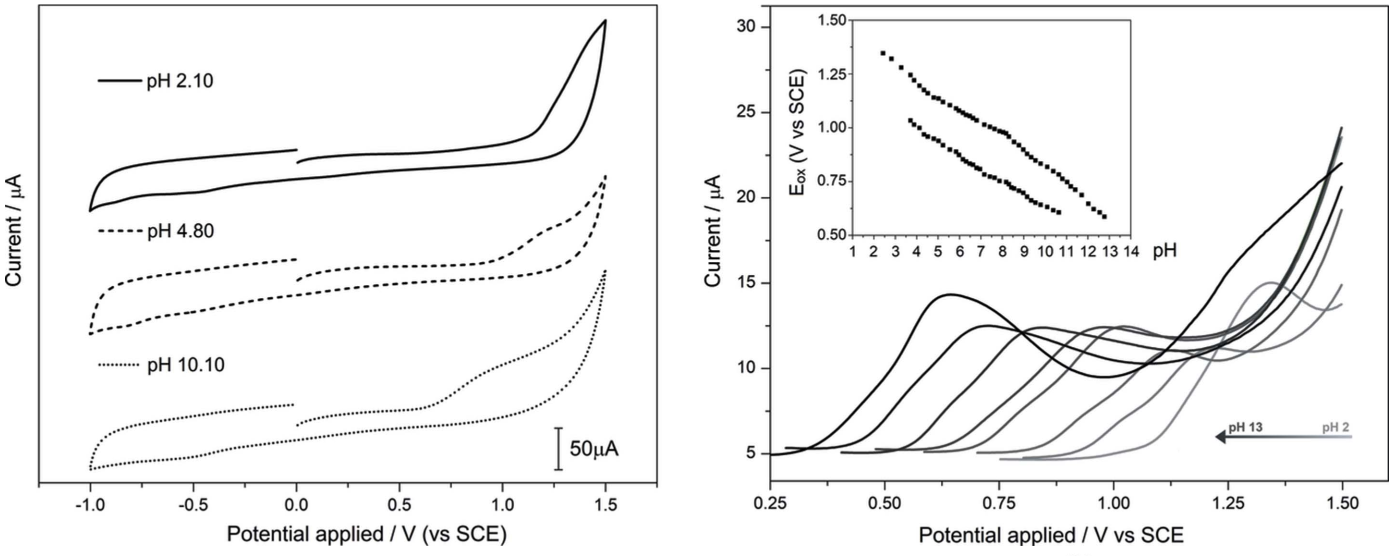

(*a*) (*b*)

Figure 10
(*a*) CVs at pHs 2.10 (solid line, predominant species H_4dimpy^{2+}), 4.80 (dashed line, predominant species H_3dimpy$^+$) and 10.10 (dotted line, predominant species H_2dimpy). (*b*) DPVs of under different pH conditions. Inset: dependence of oxidation potential (E_{ox}) as a function of pH. Conditions: H_2dimpy [1.0×10^{-3} mol l^{-1}] at 100 mV s^{-1} in aqueous 0.1 mol l^{-1} B–R buffer.

14.7, supporting our previous interpretation of the experimental results.

With the information acquired from crystal structure and pK_a data, the knowledge of acid–base equilibria in H_2dimpy led us to evaluate the electrochemical behaviour of these species. This is the first time the electrochemical behaviour of H_2dimpy has been reported, despite the extensive use of this molecule in coordination chemistry, particularly in catalysis, where the protonation/deprotonation of the ligand can change the electronic density over the metal centre and is particularly important in proton-coupled electron-transfer reactions (Okamura *et al.*, 2012).

The cyclic voltammogram of H_2dimpy at pH 5.5 is shown in Fig. 9. An irreversible oxidation process, controlled by diffusion (Fig. S19 in the supporting information) is assigned to the oxidation of H_2dimpy. The H_2dimpy irreversible electro-oxidation process starts at *ca* 993 mV with an anodic peak observed at 1.12 V. A similar electrochemical behaviour has been reported for imidazole-containing ligands (Kursakina *et al.*, 1991; Molero *et al.*, 2013; Po *et al.*, 1991).

Cyclic voltammograms (CVs) and different pulse voltammograms (DPVs) were employed to examine the dependence of the pH on the oxidation potential (E_{ox}) for H_2dimpy. A deeper analysis at the DPV showed two possible oxidation peaks, whereas the CV shows a very broad peak, assigned here to two oxidation processes, one for each individual imidazole, as already reported for similar molecules containing two imidazole groups (Akutagawa & Saito, 1995; Okamura *et al.*, 2012).

Taking into consideration the speciation with the previously determined pK_a values, CVs obtained at a pH at which the H_2dimpy, H_3dimpy$^+$ and H_4dimpy^{2+} species predominate are shown in Fig. 10(*a*), where a change in the oxidation potential upon protonation can be easily seen. Both the CVs and DPVs show similar results, as a shift of E_{ox} to lower potentials is observed when the pH is increased. Upon the first and second protonation, the observed slope at E_{ox} dependence per pH unit also changes, and close to the second protonation, only one oxidation peak is observed.

Electrochemical measurements varying small units of pH were performed in Britton–Robinson buffer as an attempt to plot a Pourbaix-like diagram, and DPVs under different pH conditions are shown in Fig. 10(*b*). Due to the irreversible behaviour caused by decomposition (Fig. S23 in the supporting information), no equilibrium between the oxidized–reduced species exists so that the inset graph in Fig. 10(*b*) only shows the dependence on the E_{ox} with the pH and no conclusion can be drawn by the slopes using the Nernst equation on the number of electrons and protons involved. DFT results (see supporting information) are in very good agreement with the electrochemical experimental data.

4. Conclusion

Our results suggest that the presence of solvent-accessible voids in the crystal structure of 2,6-bis(1*H*-imidazol-2-yl)pyridine (H_2dimpy) in compound **I** is a consequence of the formation of strong intermolecular interactions of the N—H···O and O—H···N types, along with π-stacking, which results in the crystal arrangement around the threefold axis of the trigonal space group. Additionally, the analysis of the trihydrate protonated molecule (compound **II**) confirmed the imidazole site as the protonation site. The isolation of the monoprotonated species is apparently fortuitous because the detailed investigation of the acid–base equilibria of H_2dimpy by potentiometric and spectrophotometric titration associated with DFT calculations can unequivocally confirm that two protonations take place, leading to the formation of H_3dimpy$^+$ (pK_{a1} = 5.40) and H_4dimpy^{2+} (pK_{a1} = 3.98). The combination of electrochemical, spectroelectrochemical and DFT results was used to establish that a set of two consecutive proton-coupled electron transfers combined with protonation equilibria can explain the observed electrochemical behaviour of the molecule in the full 0–14 pH range.

Acknowledgements

The authors acknowledge CENAPAD–SP (Centro Nacional de Processamento de Alto Desempenho em São Paulo) for computational time.

Funding information

Funding for this research was provided by: Fundação de Amparo à Pesquisa do Estado de São Paulo (grant Nos. 2013/22127-2, 2014/50906-9 and 2017/23960-0); Conselho Nacional de Desenvolvimento Científico e Tecnológico (studentship No. 142440/2015-9 to RBG; studentship No. 142386/2016-2 to LSCH; studentship No. 120469/2018-9 to WMG); Coordenação de Aperfeiçoamento de Pessoal de Nível Superior (studentship No. Finance Code 001 to JCT); Fundo de Apoio ao Ensino, à Pesquisa e Extensão, Universidade Estadual de Campinas (grant No. 2782/18).

References

Abbehausen, C., de Paiva, R. E. F., Formiga, A. L. B. & Corbi, P. P. (2012). *Chem. Phys.* **408**, 62–68.

Adamczyk-Woźniak, A., Cyrański, M., Durka, K., Gozdalik, J., Klimentowska, P., Rusiecki, R., Sporzyński, A. & Zarzeczańska, D. (2019). *Crystals*, **9**, 109–124.

Akutagawa, T. & Saito, G. (1995). *Bull. Chem. Soc. Jpn*, **68**, 1753–1773.

Barone, V. & Cossi, M. (1998). *J. Phys. Chem. A*, **102**, 1995–2001.

Bayar, I., Khedhiri, L., Soudani, S., Lefebvre, F., Ferretti, V. & Ben Nasr, C. (2018). *J. Mol. Struct.* **1161**, 486–496.

Becke, A. D. (1993). *J. Chem. Phys.* **98**, 5648–5652.

Bibi, N., de Arruda, E. G. R., Domingo, A., Oliveira, A. A., Galuppo, C., Phung, Q. M., Orra, N. M., Béron, F., Paesano, A. Jr, Pierloot, K. & Formiga, A. L. B. (2018*b*). *Inorg. Chem.* **57**, 14603–14616.

Bibi, N., Guerra, R. B., Huamaní, L. E. S. C. & Formiga, A. L. B. (2018*a*). *Acta Cryst.* E**74**, 874–877.

Bonacin, J. A., Formiga, A. L. B., de Melo, V. H. S. & Toma, H. E. (2007). *Vib. Spectrosc.* **44**, 133–141.

Braun, D. E., Gelbrich, T., Kahlenberg, V. & Griesser, U. J. (2015). *CrystEngComm*, **17**, 2504–2516.

Bruker (2010). *APEX3*, *SAINT* and *SADABS*. Bruker AXS Inc., Madison, Wisconsin, USA.

Carina, R. F., Verzegnassi, L., Williams, A. F. & Bernardinelli, G. (1998). *Chem. Commun.* pp. 2681–2682.

Che, C.-M., Chow, C.-F., Yuen, M.-Y., Roy, V. A. L., Lu, W., Chen, Y., Chui, S. S.-Y. & Zhu, N. (2011). *Chem. Sci.* **2**, 216–220.

Cruz Cabeza, A. J., Day, G. M., Motherwell, W. D. S. & Jones, W. (2007). *Chem. Commun.* pp. 1600–1602.

Dolomanov, O. V., Bourhis, L. J., Gildea, R. J., Howard, J. A. K. & Puschmann, H. (2009). *J. Appl. Cryst.* **42**, 339–341.

Eilbeck, W. J. & Holmes, F. (1967). *J. Chem. Soc. A*, pp. 1777–1782.

Etter, M. C. (1990). *Acc. Chem. Res.* **23**, 120–126.

Fabbiani, F. P. A., Byrne, L. T., McKinnon, J. J. & Spackman, M. A. (2007). *CrystEngComm*, **9**, 728–731.

Farrugia, L. J. (2012). *J. Appl. Cryst.* **45**, 849–854.

Fuchs, M. G. G., Dechert, S., Demeshko, S., Ryde, U. & Meyer, F. (2010). *Inorg. Chem.* **49**, 5853–5858.

Groom, C. R., Bruno, I. J., Lightfoot, M. P. & Ward, S. C. (2016). *Acta Cryst.* B**72**, 171–179.

Gutz, I. G. R. (2018). *CurTiPot 4.3.0*. University of São Paulo, Brazil, http://www.iq.usp.br/gutz/Curtipot_.html.

Halcrow, M. A. (2005). *Coord. Chem. Rev.* **249**, 2880–2908.

Hammes, B. S., Damiano, B. J., Tobash, P. H., Hidalgo, M. J. & Yap, G. P. A. (2005). *Inorg. Chem. Commun.* **8**, 513–516.

Hashiguchi, B. G., Young, K. J. H., Yousufuddin, M., Goddard, W. III & Periana, R. A. (2010). *J. Am. Chem. Soc.* **132**, 12542–12545.

Isse, A. A. & Gennaro, A. (2010). *J. Phys. Chem. B*, **114**, 7894–7899.

Izsák, R. & Neese, F. (2011). *J. Chem. Phys.* **135**, 144105.

Keith, J. A., Grice, K. A., Kubiak, C. P. & Carter, E. A. (2013). *J. Am. Chem. Soc.* **135**, 15823–15829.

Kershaw Cook, L. J., Tuna, F. & Halcrow, M. A. (2013). *Dalton Trans.* **42**, 2254–2265.

Kursakina, I. G., Starichenko, V. F., Kirilyuk, I. A., Grigor'ev, I. A. & Volodarskii, L. B. (1991). *Russ. Chem. Bull.* **40**, 1774–1778.

Latosińska, J. N., Latosińska, M., Maurin, J. K., Orzeszko, A. & Kazimierczuk, Z. (2014). *J. Phys. Chem. A*, **118**, 2089–2106.

Lee, C., Yang, W. & Parr, R. G. (1988). *Phys. Rev. B*, **37**, 785–789.

Li, L., Luo, Q., Cui, H., Li, R., Zhang, J. & Peng, T. (2018). *ChemCatChem*, **10**, 1607–1613.

Lowes, M. M. J., Caira, M. R., Lötter, A. P. & Van Der Watt, J. G. (1987). *J. Pharm. Sci.* **76**, 744–752.

Macrae, C. F., Bruno, I. J., Chisholm, J. A., Edgington, P. R., McCabe, P., Pidcock, E., Rodriguez-Monge, L., Taylor, R., van de Streek, J. & Wood, P. A. (2008). *J. Appl. Cryst.* **41**, 466–470.

McKinnon, J. J., Spackman, M. A. & Mitchell, A. S. (2004). *Acta Cryst.* B**60**, 627–668.

Molero, L., Faundez, M., Valle, M. A., del Río, R. & Armijo, F. (2013). *Electrochim. Acta*, **88**, 871–876.

Neese, F. (2012). *WIREs Comput. Mol. Sci.* **2**, 73–78.

Okamura, M., Yoshida, M., Kuga, R., Sakai, K., Kondo, M. & Masaoka, S. (2012). *Dalton Trans.* **41**, 13081–13089.

Parsons, S., Flack, H. D. & Wagner, T. (2013). *Acta Cryst.* B**69**, 249–259.

Po, H. N., Shariff, Z., Masse, J. A., Freeman, F. & Keindl-yu, M. C. (1991). *Phosphorus Sulfur Silicon*, **63**, 1–12.

Ratier de Arruda, E. G., de Farias, M. A., Venturinelli Jannuzzi, S. A., de Almeida Gonsales, S., Timm, R. A., Sharma, S., Zoppellaro, G., Kubota, L. T., Knobel, M. & Barboza Formiga, A. L. (2017). *Inorg. Chim. Acta*, **466**, 456–463.

Rigsby, M. L., Mandal, S., Nam, W., Spencer, L. C., Llobet, A. & Stahl, S. S. (2012). *Chem. Sci.* **3**, 3058–3062.

Savchuk, M. O., Litsis, O. O., Znovjyak, K. O., Sliva, T. Yu., Kobylinskaya, N. G., Shishkina, S. V., Dyakonenko, V. V. & Amirkhanov, V. M. (2017). *Polyhedron*, **133**, 162–168.

Sheldrick, G. M. (2015*a*). *Acta Cryst.* A**71**, 3–8.

Sheldrick, G. M. (2015*b*). *Acta Cryst.* C**71**, 3–8.

Spackman, M. A. & Jayatilaka, D. (2009). *CrystEngComm*, **11**, 19–32.

Spackman, M. A. & McKinnon, J. J. (2002). *CrystEngComm*, **4**, 378–392.

Spek, A. L. (2009). *Acta Cryst.* D**65**, 148–155.

Spek, A. L. (2015). *Acta Cryst.* C**71**, 9–18.

Stupka, G., Gremaud, L., Bernardinelli, G. & Williams, A. F. (2004). *Dalton Trans.* pp. 407–412.

Taylor, D. E. & Sausa, R. C. (2018). *J. Mol. Struct.* **1162**, 45–53.

Timm, R. A., Bonacin, J. A., Formiga, A. L. B. & Toma, H. E. (2008). *J. Braz. Chem. Soc.* **19**, 287–292.

Turner, M. J., McKinnon, J. J., Wolff, S. K., Grimwood, D. J., Spackman, P. R., Jayatilaka, D. & Spackman, M. A. (2017). *CrystalExplorer17*. University of Western Australia. http://hirshfeldsurface.net/.

Voss, M. E., Beer, C. M., Mitchell, S. A., Blomgren, P. A. & Zhichkin, P. E. (2008). *Tetrahedron*, **64**, 645–651.

Weigend, F. (2006). *Phys. Chem. Chem. Phys.* **8**, 1057–1065.

Weigend, F. & Ahlrichs, R. (2005). *Phys. Chem. Chem. Phys.* **7**, 3297–3305.

Zeman, S., Roháč, M., Friedl, Z., Růžička, A. & Lyčka, A. (2010). *Propellants Explosives Pyrotech.* **35**, 130–135.

Zou, T., Lum, C. T., Chui, S. S.-Y. & Che, C.-M. (2013). *Angew. Chem. Int. Ed.* **52**, 2930–2933.

supporting information

Acta Cryst. (2019). C**75**, 1359-1371 [https://doi.org/10.1107/S2053229619011951]

Analysis of solvent-accessible voids and proton-coupled electron transfer of 2,6-bis(1*H*-imidazol-2-yl)pyridine and its hydrochloride

Renan B. Guerra, Luis S. C. Huamaní, Juan C. Tenorio, Willian M. Guimarães, Juliano A. Bonacin and André Luiz Barboza Formiga

Computing details

For both structures, data collection: *APEX3* (Bruker, 2010); cell refinement: *SAINT* (Bruker, 2010); data reduction: *SAINT* (Bruker, 2010); program(s) used to solve structure: SHELXT (Sheldrick, 2015a); program(s) used to refine structure: *SHELXL2018* (Sheldrick, 2015b); molecular graphics: OLEX2 (Dolomanov *et al.*, 2009) and *ORTEP-3* (Farrugia, 2012); software used to prepare material for publication: OLEX2 (Dolomanov *et al.*, 2009) and *Mercury* (Macrae *et al.*, 2008).

2,6-Bis(1*H*-imidazol-2-yl)pyridine trihydrate (H2dimpyl)

Crystal data

$C_{11}H_9N_5\cdot3H_2O\cdot$[+solvent]
$M_r = 265.28$
Trigonal, $P3_221$
$a = 18.6043$ (5) Å
$c = 3.9112$ (1) Å
$V = 1172.38$ (7) Å^3
$Z = 3$
$F(000) = 420$
$D_x = 1.127$ Mg m^{-3}
Cu $K\alpha$ radiation, $\lambda = 1.54178$ Å
Cell parameters from 3604 reflections
$\theta = 2.7$–$68.5°$
$\mu = 0.71$ mm^{-1}
$T = 150$ K
Needle, colourless
0.42 × 0.07 × 0.06 mm

Data collection

Bruker APEX CCD detector diffractometer
Radiation source: fine-focus sealed tube
Detector resolution: 8.3333 pixels mm^{-1}
φ and ω scans
Absorption correction: multi-scan (SADABS; Bruker, 2010)
$T_{min} = 0.589$, $T_{max} = 0.753$
4574 measured reflections
1416 independent reflections
1375 reflections with $I > 2\sigma(I)$
$R_{int} = 0.035$
$\theta_{max} = 68.5°$, $\theta_{min} = 2.7°$
$h = -22 \rightarrow 22$
$k = -21 \rightarrow 11$
$l = -4 \rightarrow 4$

Refinement

Refinement on F^2
Least-squares matrix: full
$R[F^2 > 2\sigma(F^2)] = 0.038$
$wR(F^2) = 0.095$
$S = 1.12$
1416 reflections
107 parameters
13 restraints
Primary atom site location: dual
Hydrogen site location: mixed
H-atom parameters constrained
$w = 1/[\sigma^2(F_o^2) + (0.0717P)^2 + 0.0039P]$ where $P = (F_o^2 + 2F_c^2)/3$
$(\Delta/\sigma)_{max} < 0.001$
$\Delta\rho_{max} = 0.19$ e Å^{-3}
$\Delta\rho_{min} = -0.18$ e Å^{-3}

Absolute structure: Flack *x* determined using 610 quotients [(I+)-(I-)]/[(I+)+(I-)] (Parsons *et al.*, 2013)
Absolute structure parameter: −0.06 (13)

Special details

Geometry. All esds (except the esd in the dihedral angle between two l.s. planes) are estimated using the full covariance matrix. The cell esds are taken into account individually in the estimation of esds in distances, angles and torsion angles; correlations between esds in cell parameters are only used when they are defined by crystal symmetry. An approximate (isotropic) treatment of cell esds is used for estimating esds involving l.s. planes.

Fractional atomic coordinates and isotropic or equivalent isotropic displacement parameters (Å²)

	x	*y*	*z*	U_{iso}*/U_{eq}	Occ. (<1)
C1	0.82009 (12)	0.40541 (14)	0.3290 (4)	0.0424 (5)	
H1	0.810118	0.449603	0.278080	0.051*	
C2	0.77089 (11)	0.32375 (13)	0.2485 (4)	0.0439 (5)	
H2	0.719764	0.301261	0.128372	0.053*	
C3	0.87644 (11)	0.33371 (12)	0.5186 (4)	0.0376 (4)	
C4	0.93872 (11)	0.31921 (12)	0.6842 (4)	0.0393 (5)	
C5	0.93498 (13)	0.24231 (13)	0.6823 (5)	0.0488 (5)	
H5	0.889499	0.195000	0.581093	0.059*	
C6	1.000000	0.23727 (18)	0.833333	0.0563 (7)	
H6	1.000000	0.186204	0.833331	0.068*	
N1	0.88686 (9)	0.41061 (10)	0.4985 (3)	0.0371 (4)	
H1A	0.929205	0.456226	0.580214	0.045*	
N2	0.80616 (10)	0.27824 (10)	0.3670 (4)	0.0434 (4)	
N3	1.000000	0.38611 (12)	0.833333	0.0357 (5)	
O1	1.000000	0.56592 (11)	0.833333	0.0498 (5)	
H1B	0.984190	0.590942	0.977527	0.075*	
O2B	0.7265 (2)	0.1091 (2)	0.420 (4)	0.126 (4)	0.710 (16)
H2BA	0.753917	0.088908	0.317271	0.189*	0.710 (16)
H2BB	0.762778	0.161343	0.450509	0.189*	0.710 (16)
O2A	0.7301 (4)	0.1159 (4)	0.160 (3)	0.059 (3)	0.290 (16)
H2AA	0.735540	0.091151	−0.018624	0.089*	0.290 (16)
H2AB	0.770014	0.167082	0.141571	0.089*	0.290 (16)

Atomic displacement parameters (Å²)

	U^{11}	U^{22}	U^{33}	U^{12}	U^{13}	U^{23}
C1	0.0340 (9)	0.0561 (12)	0.0319 (7)	0.0187 (9)	0.0036 (6)	0.0041 (7)
C2	0.0340 (9)	0.0572 (12)	0.0333 (8)	0.0175 (8)	0.0007 (6)	−0.0024 (7)
C3	0.0302 (8)	0.0444 (9)	0.0303 (8)	0.0126 (7)	0.0070 (6)	−0.0016 (6)
C4	0.0334 (9)	0.0448 (10)	0.0336 (8)	0.0150 (8)	0.0094 (7)	0.0010 (7)
C5	0.0433 (12)	0.0431 (10)	0.0536 (11)	0.0167 (9)	0.0053 (9)	−0.0019 (8)
C6	0.0581 (18)	0.0482 (11)	0.0658 (17)	0.0291 (9)	0.0001 (14)	0.0001 (7)
N1	0.0275 (7)	0.0437 (8)	0.0320 (6)	0.0117 (6)	0.0047 (5)	0.0009 (6)
N2	0.0343 (7)	0.0484 (9)	0.0364 (7)	0.0122 (7)	0.0029 (5)	−0.0061 (6)
N3	0.0298 (10)	0.0420 (9)	0.0312 (9)	0.0149 (5)	0.0072 (7)	0.0036 (3)

O1	0.0377 (10)	0.0433 (8)	0.0665 (13)	0.0189 (5)	−0.0007 (8)	−0.0004 (4)
O2B	0.0570 (19)	0.0463 (17)	0.261 (13)	0.0153 (14)	−0.052 (4)	−0.027 (3)
O2A	0.049 (3)	0.040 (3)	0.084 (6)	0.019 (2)	−0.024 (3)	−0.014 (3)

Geometric parameters (Å, º)

C1—H1	0.9500	C5—H5	0.9500
C1—C2	1.362 (3)	C5—C6	1.391 (3)
C1—N1	1.368 (3)	C6—H6	0.9500
C2—H2	0.9500	N1—H1A	0.8800
C2—N2	1.385 (3)	O1—H1B^{i}	0.87
C3—C4	1.465 (3)	O1—H1B	0.8708
C3—N1	1.347 (3)	O2B—H2BA	0.8693
C3—N2	1.333 (3)	O2B—H2BB	0.8699
C4—C5	1.397 (3)	O2A—H2AA	0.8711
C4—N3	1.330 (2)	O2A—H2AB	0.8700
C2—C1—H1	127.1	C6—C5—C4	117.8 (2)
C2—C1—N1	105.72 (18)	C6—C5—H5	121.1
N1—C1—H1	127.1	C5^{i}—C6—C5	119.7 (3)
C1—C2—H2	124.9	C5^{i}—C6—H6	120.2
C1—C2—N2	110.18 (16)	C5—C6—H6	120.2
N2—C2—H2	124.9	C1—N1—H1A	126.0
N1—C3—C4	120.95 (17)	C3—N1—C1	108.06 (16)
N2—C3—C4	127.88 (18)	C3—N1—H1A	126.0
N2—C3—N1	111.15 (18)	C3—N2—C2	104.88 (16)
C5—C4—C3	123.15 (18)	C4—N3—C4^{i}	119.1 (2)
N3—C4—C3	114.09 (18)	H1B—O1—H1B^{i}	90.6
N3—C4—C5	122.75 (18)	H2BA—O2B—H2BB	104.6
C4—C5—H5	121.1	H2AA—O2A—H2AB	104.4
C1—C2—N2—C3	0.12 (19)	N1—C1—C2—N2	0.22 (19)
C2—C1—N1—C3	−0.47 (17)	N1—C3—C4—C5	−173.49 (15)
C3—C4—C5—C6	176.78 (13)	N1—C3—C4—N3	5.7 (2)
C3—C4—N3—C4^{i}	−177.97 (15)	N1—C3—N2—C2	−0.43 (17)
C4—C3—N1—C1	179.33 (14)	N2—C3—C4—C5	5.0 (3)
C4—C3—N2—C2	−179.08 (15)	N2—C3—C4—N3	−175.81 (13)
C4—C5—C6—C5^{i}	1.07 (11)	N2—C3—N1—C1	0.58 (17)
C5—C4—N3—C4^{i}	1.18 (12)	N3—C4—C5—C6	−2.3 (2)

Symmetry code: (i) −*x*+2, −*x*+*y*+1, −*z*+5/3.

Hydrogen-bond geometry (Å, º)

D—H···*A*	*D*—H	H···*A*	*D*···*A*	*D*—H···*A*
N1—H1*A*···O1	0.88	2.05	2.900 (2)	163
O1—H1*B*···O2*B*^{ii}	0.87	2.07	2.823 (5)	144
O1—H1*B*···O2*A*^{ii}	0.87	2.19	2.719 (7)	119

O2*B*—H2*BB*···N2	0.87	1.93	2.734 (4)	153
O2*A*—H2*AB*···N2	0.87	2.03	2.740 (7)	138

Symmetry code: (ii) $-y+1, x-y, z+2/3$.

2-[6-(1*H*-Imidazol-2-yl)pyridin-2-yl]-1*H*-imidazol-3-ium chloride trihydrate (II)

Crystal data

$C_{11}H_{10}N_5^+\cdot Cl^-\cdot 3H_2O$
$M_r = 301.74$
Monoclinic, $P2_1/c$
$a = 6.6577$ (5) Å
$b = 22.6308$ (16) Å
$c = 9.7566$ (7) Å
$\beta = 103.845$ (3)°
$V = 1427.31$ (18) Å^3
$Z = 4$
$F(000) = 632$
$D_x = 1.404$ Mg m^{-3}
Cu $K\alpha$ radiation, $\lambda = 1.54178$ Å
Cell parameters from 51 reflections
$\theta = 2.4$–19.1°
$\mu = 2.53$ mm^{-1}
$T = 150$ K
Needle, colorless
0.21 × 0.12 × 0.06 mm

Data collection

Bruker APEX CCD detector diffractometer
Detector resolution: 8.3333 pixels mm^{-1}
phi and ω scans
Absorption correction: multi-scan (SADABS; Bruker, 2010)
$T_{min} = 0.541$, $T_{max} = 0.753$
12948 measured reflections
2501 independent reflections
2337 reflections with $I > 2\sigma(I)$
$R_{int} = 0.037$
$\theta_{max} = 66.6°$, $\theta_{min} = 3.9°$
$h = -7 \rightarrow 7$
$k = -26 \rightarrow 26$
$l = -10 \rightarrow 11$

Refinement

Refinement on F^2
Least-squares matrix: full
$R[F^2 > 2\sigma(F^2)] = 0.030$
$wR(F^2) = 0.083$
$S = 1.08$
2501 reflections
208 parameters
0 restraints
Primary atom site location: dual
Hydrogen site location: mixed
H atoms treated by a mixture of independent and constrained refinement
$w = 1/[\sigma^2(F_o^2) + (0.0446P)^2 + 0.3908P]$ where $P = (F_o^2 + 2F_c^2)/3$
$(\Delta/\sigma)_{max} < 0.001$
$\Delta\rho_{max} = 0.19$ e Å^{-3}
$\Delta\rho_{min} = -0.25$ e Å^{-3}

Special details

Geometry. All esds (except the esd in the dihedral angle between two l.s. planes) are estimated using the full covariance matrix. The cell esds are taken into account individually in the estimation of esds in distances, angles and torsion angles; correlations between esds in cell parameters are only used when they are defined by crystal symmetry. An approximate (isotropic) treatment of cell esds is used for estimating esds involving l.s. planes.

Fractional atomic coordinates and isotropic or equivalent isotropic displacement parameters (Å^2)

	x	*y*	*z*	U_{iso}*/U_{eq}
Cl1	0.12492 (5)	0.11289 (2)	0.19035 (3)	0.02985 (13)
N1	0.23324 (18)	0.15345 (5)	0.50852 (13)	0.0242 (3)
H1	0.209 (3)	0.1367 (8)	0.4320 (19)	0.029*
N2	0.32601 (18)	0.16788 (5)	0.73294 (13)	0.0238 (3)
H2	0.363 (2)	0.1621 (8)	0.8221 (19)	0.029*
N3	0.25814 (16)	0.03224 (5)	0.52905 (12)	0.0207 (2)

N4	0.16978 (18)	−0.02797 (6)	0.27592 (13)	0.0264 (3)
H4	0.164 (3)	0.0095 (8)	0.2606 (19)	0.032*
N5	0.21873 (18)	−0.11532 (5)	0.38022 (14)	0.0284 (3)
C1	0.2362 (2)	0.21322 (6)	0.52931 (16)	0.0301 (3)
H1A	0.202959	0.242704	0.458158	0.036*
C2	0.2952 (2)	0.22247 (6)	0.66969 (16)	0.0292 (3)
H2A	0.312323	0.259679	0.716116	0.035*
C3	0.28748 (19)	0.12627 (6)	0.63302 (14)	0.0211 (3)
C4	0.29992 (18)	0.06222 (6)	0.65134 (14)	0.0203 (3)
C5	0.3499 (2)	0.03559 (6)	0.78353 (15)	0.0253 (3)
H5	0.377869	0.058487	0.867563	0.030*
C6	0.3575 (2)	−0.02556 (6)	0.78827 (16)	0.0293 (3)
H6	0.390061	−0.045476	0.876542	0.035*
C7	0.3175 (2)	−0.05737 (6)	0.66416 (15)	0.0271 (3)
H7	0.324146	−0.099307	0.665627	0.032*
C8	0.26720 (19)	−0.02676 (6)	0.53637 (15)	0.0217 (3)
C9	0.21986 (19)	−0.05725 (6)	0.40025 (15)	0.0231 (3)
C10	0.1339 (2)	−0.06927 (7)	0.17056 (16)	0.0316 (3)
H10	0.095412	−0.062150	0.071766	0.038*
C11	0.1645 (2)	−0.12247 (7)	0.23613 (17)	0.0326 (4)
H11	0.150535	−0.159532	0.189061	0.039*
O1	0.70136 (19)	0.21532 (5)	0.43975 (13)	0.0386 (3)
H1B	0.726 (3)	0.2432 (10)	0.503 (2)	0.058*
H1C	0.728 (3)	0.1862 (10)	0.494 (2)	0.058*
O2	0.4310 (2)	0.14867 (5)	0.01164 (11)	0.0345 (3)
H2B	0.344 (3)	0.1399 (9)	0.064 (2)	0.052*
H2C	0.531 (3)	0.1656 (10)	0.063 (2)	0.052*
O3	0.76769 (18)	0.20389 (5)	0.17490 (12)	0.0348 (3)
H3A	0.868 (3)	0.1834 (10)	0.182 (2)	0.052*
H3B	0.756 (3)	0.2116 (9)	0.259 (2)	0.052*

Atomic displacement parameters (Å^2)

	U^{11}	U^{22}	U^{33}	U^{12}	U^{13}	U^{23}
Cl1	0.0355 (2)	0.0303 (2)	0.0229 (2)	0.00122 (13)	0.00543 (15)	0.00105 (13)
N1	0.0294 (6)	0.0225 (6)	0.0205 (6)	−0.0018 (5)	0.0054 (5)	−0.0005 (5)
N2	0.0294 (6)	0.0204 (6)	0.0220 (6)	−0.0016 (4)	0.0067 (5)	−0.0017 (5)
N3	0.0171 (5)	0.0209 (6)	0.0236 (6)	−0.0005 (4)	0.0040 (4)	−0.0009 (4)
N4	0.0261 (6)	0.0254 (6)	0.0267 (6)	−0.0006 (5)	0.0042 (5)	−0.0039 (5)
N5	0.0262 (6)	0.0233 (6)	0.0360 (7)	−0.0026 (4)	0.0076 (5)	−0.0072 (5)
C1	0.0390 (8)	0.0205 (7)	0.0318 (8)	−0.0010 (6)	0.0107 (6)	0.0046 (6)
C2	0.0387 (8)	0.0181 (7)	0.0329 (8)	−0.0027 (6)	0.0128 (6)	−0.0016 (6)
C3	0.0180 (6)	0.0233 (7)	0.0224 (7)	−0.0008 (5)	0.0055 (5)	−0.0009 (5)
C4	0.0155 (6)	0.0215 (7)	0.0235 (7)	−0.0002 (5)	0.0041 (5)	−0.0016 (5)
C5	0.0258 (7)	0.0257 (7)	0.0227 (7)	0.0008 (5)	0.0026 (5)	−0.0009 (6)
C6	0.0341 (8)	0.0262 (7)	0.0258 (7)	0.0018 (6)	0.0035 (6)	0.0054 (6)
C7	0.0286 (7)	0.0198 (6)	0.0312 (8)	0.0008 (5)	0.0042 (6)	0.0012 (6)
C8	0.0151 (6)	0.0219 (7)	0.0280 (7)	−0.0009 (5)	0.0050 (5)	−0.0022 (5)

C9	0.0177 (6)	0.0228 (6)	0.0284 (7)	−0.0015 (5)	0.0049 (5)	−0.0025 (6)
C10	0.0289 (8)	0.0388 (9)	0.0264 (8)	−0.0030 (6)	0.0051 (6)	−0.0106 (6)
C11	0.0284 (7)	0.0308 (8)	0.0381 (9)	−0.0041 (6)	0.0071 (7)	−0.0148 (7)
O1	0.0539 (7)	0.0298 (6)	0.0310 (6)	0.0030 (5)	0.0083 (5)	−0.0031 (5)
O2	0.0469 (7)	0.0338 (6)	0.0238 (5)	−0.0080 (5)	0.0101 (5)	−0.0031 (4)
O3	0.0395 (6)	0.0338 (6)	0.0305 (6)	0.0071 (5)	0.0073 (5)	0.0053 (5)

Geometric parameters (Å, º)

N1—H1	0.818 (18)	C4—C5	1.3899 (19)
N1—C1	1.3672 (18)	C5—H5	0.9500
N1—C3	1.3321 (18)	C5—C6	1.385 (2)
N2—H2	0.856 (18)	C6—H6	0.9500
N2—C2	1.3742 (19)	C6—C7	1.379 (2)
N2—C3	1.3354 (18)	C7—H7	0.9500
N3—C4	1.3426 (17)	C7—C8	1.395 (2)
N3—C8	1.3376 (17)	C8—C9	1.4625 (19)
N4—H4	0.861 (19)	C10—H10	0.9500
N4—C9	1.3521 (19)	C10—C11	1.356 (2)
N4—C10	1.3674 (19)	C11—H11	0.9500
N5—C9	1.3286 (18)	O1—H1B	0.87 (2)
N5—C11	1.375 (2)	O1—H1C	0.84 (2)
C1—H1A	0.9500	O2—H2B	0.88 (2)
C1—C2	1.348 (2)	O2—H2C	0.82 (2)
C2—H2A	0.9500	O3—H3A	0.80 (2)
C3—C4	1.4604 (18)	O3—H3B	0.86 (2)

C1—N1—H1	125.9 (12)	C6—C5—C4	117.58 (13)
C3—N1—H1	124.8 (12)	C6—C5—H5	121.2
C3—N1—C1	109.29 (12)	C5—C6—H6	120.2
C2—N2—H2	124.7 (12)	C7—C6—C5	119.63 (13)
C3—N2—H2	126.3 (12)	C7—C6—H6	120.2
C3—N2—C2	108.91 (12)	C6—C7—H7	120.7
C8—N3—C4	117.38 (12)	C6—C7—C8	118.69 (13)
C9—N4—H4	129.1 (12)	C8—C7—H7	120.7
C9—N4—C10	107.50 (13)	N3—C8—C7	122.78 (13)
C10—N4—H4	123.4 (12)	N3—C8—C9	115.17 (12)
C9—N5—C11	104.94 (12)	C7—C8—C9	122.05 (12)
N1—C1—H1A	126.4	N4—C9—C8	122.47 (12)
C2—C1—N1	107.14 (13)	N5—C9—N4	111.18 (12)
C2—C1—H1A	126.4	N5—C9—C8	126.35 (13)
N2—C2—H2A	126.5	N4—C10—H10	127.1
C1—C2—N2	107.02 (12)	C11—C10—N4	105.83 (14)
C1—C2—H2A	126.5	C11—C10—H10	127.1
N1—C3—N2	107.63 (12)	N5—C11—H11	124.7
N1—C3—C4	124.40 (12)	C10—C11—N5	110.55 (13)
N2—C3—C4	127.97 (12)	C10—C11—H11	124.7
N3—C4—C3	113.53 (12)	H1B—O1—H1C	99 (2)

N3—C4—C5	123.93 (12)	H2B—O2—H2C	107 (2)
C5—C4—C3	122.54 (12)	H3A—O3—H3B	107 (2)
C4—C5—H5	121.2		

N1—C1—C2—N2	−0.46 (17)	C4—N3—C8—C7	0.00 (19)
N1—C3—C4—N3	2.26 (18)	C4—N3—C8—C9	179.85 (11)
N1—C3—C4—C5	−177.58 (12)	C4—C5—C6—C7	0.5 (2)
N2—C3—C4—N3	−177.85 (12)	C5—C6—C7—C8	−0.9 (2)
N2—C3—C4—C5	2.3 (2)	C6—C7—C8—N3	0.7 (2)
N3—C4—C5—C6	0.3 (2)	C6—C7—C8—C9	−179.12 (12)
N3—C8—C9—N4	−0.23 (18)	C7—C8—C9—N4	179.61 (13)
N3—C8—C9—N5	179.97 (12)	C7—C8—C9—N5	−0.2 (2)
N4—C10—C11—N5	0.03 (16)	C8—N3—C4—C3	179.65 (11)
C1—N1—C3—N2	−0.29 (15)	C8—N3—C4—C5	−0.51 (18)
C1—N1—C3—C4	179.62 (12)	C9—N4—C10—C11	−0.15 (15)
C2—N2—C3—N1	0.00 (15)	C9—N5—C11—C10	0.10 (16)
C2—N2—C3—C4	−179.91 (13)	C10—N4—C9—N5	0.22 (15)
C3—N1—C1—C2	0.48 (17)	C10—N4—C9—C8	−179.60 (12)
C3—N2—C2—C1	0.29 (16)	C11—N5—C9—N4	−0.20 (15)
C3—C4—C5—C6	−179.91 (12)	C11—N5—C9—C8	179.62 (13)

Hydrogen-bond geometry (Å, º)

D—H···*A*	*D*—H	H···*A*	*D*···*A*	*D*—H···*A*
N1—H1···Cl1	0.82 (2)	2.35 (2)	3.1508 (13)	166 (2)
N2—H2···O2^{i}	0.86 (2)	1.82 (2)	2.6762 (17)	178 (2)
N4—H4···Cl1	0.86 (2)	2.43 (2)	3.2907 (13)	174 (2)
O1—H1*B*···O3^{ii}	0.87 (2)	2.03 (2)	2.8839 (16)	169 (2)
O1—H1*C*···N5^{iii}	0.84 (2)	2.00 (2)	2.8359 (18)	178 (2)
O2—H2*B*···Cl1	0.88 (2)	2.21 (2)	3.0900 (13)	177 (2)
O2—H2*C*···O3	0.82 (2)	1.90 (2)	2.7230 (17)	177 (2)
O3—H3*A*···Cl1^{iv}	0.80 (2)	2.33 (2)	3.1223 (12)	171 (2)
O3—H3*B*···O1	0.86 (2)	1.89 (2)	2.7359 (17)	169 (2)

Symmetry codes: (i) *x*, *y*, *z*+1; (ii) *x*, −*y*+1/2, *z*+1/2; (iii) −*x*+1, −*y*, −*z*+1; (iv) *x*+1, *y*, *z*.